Thesis for the degree of Doctor of Philosophy

Local structure and dynamics of proton and hydride-ion conducting perovskite type oxides

LAURA MAZZEI

CHALMERS

Department of Physics

Chalmers University of Technology

Gothenburg, Sweden 2019

Local structure and dynamics of proton and hydride-ion conducting perovskite type oxides

LAURA MAZZEI

ISBN 978-91-7905-110-5

Doktorsavhandlingar vid Chalmers tekniska hgskola
Ny serie nr 4577
ISSN 0346-718X

Department of Physics
Chalmers University of Technology
SE-412 96 Göteborg, Sweden

Cover: Artistic interpretation of the hydrogen dynamics in the perovskite oxide structure

Printed by Chalmers Reproservice AB
Göteborg, 2019

Local structure and dynamics of proton and hydride-ion conducting perovskite type oxides

Laura Mazzei
Department of Physics
Chalmers University of Technology

Abstract

Proton and hydride-ion conducting oxides show potential for application in several technological devices, such as solid oxide fuel cells and batteries. However, fundamental properties pertaining to the local structure and conduction mechanisms in these materials are unclear. Such fundamental knowledge is crucial for the development of novel materials and, ultimately, for their application in technological devices. This thesis reports on investigations of local structure and dynamics in two families of hydrogen containing perovskite structured oxides, namely proton-conducting $BaZr_xM_{1-x}O_3H_x$ (M = In, Sc and Y, $x \leq 0.5$) and hydride-ion conducting $BaTiO_{3-x}H_x$ ($x \leq 0.15$).

For the proton conducting $BaZr_xM_{1-x}O_3H_x$ materials, the investigations focused on the nature of the proton sites in polycrystalline powder samples and were performed using inelastic neutron scattering and infrared and Raman spectroscopy combined with computer simulations. The results reveal the presence of a distribution of different types of proton sites, which were virtually the same for all chemical compositions except for a high level ($x \geq 0.5$) of In-doping. It is argued that the high In-doping results in the presence of additional proton sites located in distorted structural arrangements and which resemble those found in the hydrated form of the brownmillerite structured $Ba_2In_2O_5$ system. It is also shown that the local environment for a specific proton changes over time due to the lattice vibrational dynamics. Additionally, thin-film samples were investigated by means of X-ray and neutron reflectivity and nuclear reaction analysis, with the aim to obtain details about the incorporation and distribution of protons in the samples. A key result is the observation of a thin (3-4 nm) proton-rich layer near to the surface of the films. This layer features proton sites characterized by relatively week hydrogen-bond interactions and a reduced proton mobility compared to the bulk of the film.

The studies on hydride-ion conducting $BaTiO_{3-x}H_x$ materials focused on revealing the nature of the local environments of the hydride ions and were performed using inelastic neutron scattering techniques and computer simulations. It is found that the presence of oxygen vacancies in the proximity of the hydride ions significantly influences their local environments and the vibrational properties.

Keywords: *Perovskite oxides, hydrogen, vibrational dynamics, local coordination, thin films, vibrational spectroscopy, neutron scattering.*

LIST OF PUBLICATIONS

This thesis is based on the following publications

I **Local structure and vibrational dynamics in indium-doped barium zirconate**
L. Mazzei, A. Perrichon, A. Mancini, G. Wahnström, L. Malavasi, S. F. Parker, L. Börjesson, M. Karlsson.
J. Mater. Chem. A, vol. 7, pp. 7360-7372, 2019 (Front Cover);

II **Local coordination of protons in acceptor doped barium zirconates**
L. Mazzei, A. Perrichon, A. Mancini, L. Malavasi, S. F. Parker, L. Börjesson, M. Karlsson.
In manuscript;

III **Local structure and vibrational dynamics of metal hydride reduced $BaTiO_3$**
C. Eklöf-Österberg, L. Mazzei, E. Jedvik Granhed, G. Wahnström, R. Nedumkandathil, U. Häussermann, S. F. Parker, N. H. Jalarvo, L. Börjesson, M. Karlsson.
In manuscript ;

IV **Structure and Conductivity of Epitaxial Thin Films of In-Doped $BaZrO_3$ - Based Proton Conductors**
L. Mazzei, M. Wolff, D. Pergolesi, J. A. Dura, L. Börjesson, P. Gutfreund, M. Bettinelli, T. Lippert, and M. Karlsson.
J. Phys. Chem. C, vol. 120, pp. 28415-28422, 2016 (Front Cover);

V **Phonon spectra of pure and acceptor doped $BaZrO_3$ investigated with resonance Raman spectroscopy**
L. Mazzei, B. Grimm-Lebsanft, D. Rukser, F. Biebl, J. Andreasson, D. Pergolesi, L. Börjesson, M. A. Rübhausen, T. Lippert and M. Karlsson.
In manuscript ;

Additional publications not included in this thesis

VI **Structure and dehydration mechanism of the proton conducting oxide $Ba_2In_2O_5(H_2O)_x$**
J. Bielecki, S. F. Parker, L. Mazzei, L. Börjesson, M. Karlsson
J. Mater. Chem. A, vol. 4, pp. 1224-1232, 2016 (Front Cover).

THE AUTHOR'S CONTRIBUTION TO THE PAPERS

Paper I I performed the INS experiment, the IR spectroscopy and TGA measurements, the data analysis and wrote the corresponding sections of the paper. I contributed to the interpretation of the results and was the main responsible for the writing of the paper.

Paper II I performed the INS experiment, the IR and Raman spectroscopy and TGA measurements and the data analysis, and wrote the corresponding sections of the paper. I contributed to the interpretation of the results and was the main responsible for the writing of the paper.

Paper III I contributed to the INS experiment, data analysis and interpretation and I was responsible for the writing of the corresponding sections in the paper.

Paper IV I performed the NR experiments and participate to the IS, NRA and XRR experiments. I was the main responsible for the analysis of all the experimental data, the interpretation of the results and the writing of the paper.

Paper V I participated in the resonance Raman experiment and I performed the analysis of the measured Raman spectra. I was the main responsible for the interpretation of the results and the writing of the paper.

Contents

Glossary

Abbreviations

AIMD	*Ab initio* molecular dynamics
eSDL / nSLD	Electronic / neutron scattering length density
INS	Inelastic neutron scattering
IR	Infrared
MSD	Mean square displacement
NMR	Nuclear magnetic resonance
NR	Neutron reflectivity
NRA	Nuclear reaction analysis
QENS	Quasielastic neutron scattering
SOFC	Solid oxide fuel cell
TOF	Time of flight
XRR	X-ray reflectivity

Symbols

b_{coh}, b_{inc}, b_{tot}	Coherent, incoherent and total neutron scattering length
δ(O-H), ν(O-H)	O-H bend, O-H stretch
σ_{coh}, σ_{inc}, σ_{tot}	Coherent, incoherent and total neutron scattering cross section
BZO	$BaZrO_3$
BTO	$BaTiO_3$
10In/BZO	10% In-doped $BaZrO_3$
10Sc/BZO	10% Sc-doped $BaZrO_3$
20YBZO	20% Y-doped $BaZrO_3$
47In/BZO	47% In-doped $BaZrO_3$
50In/BZO	50% In-doped $BaZrO_3$
50Sc/BZO	50% Sc-doped $BaZrO_3$

Chapter 1

Introduction

The study of the local coordination and dynamics of hydrogen species in materials is an important area of research due to the commonly strong correlation of the macroscopic properties of materials and their local structure and dynamics. Examples include very diverse phenomena encompassing different scientific areas, such as the role of hydrogen in water state transitions and supercooled states [1], protein binding affinity [2,3], DNA dynamics [4], photosynthesis [5], molecular self-assembly or catalysis [6] and proton conductivity [7–10].

Of specific concern of this thesis is the study of local coordination environments of hydrogen atoms in perovskite type oxides, with a focus on proton conducting oxides. These materials have received considerable attention mainly due to their potential application as electrolytes in fuel cells [9, 11–16], but also in other devices such as hydrogen sensors [14, 17], membranes for hydrogen separation [18,19], steam electrolyzers [20] and membrane reactors [14,21]. Fuel cells, in particular, represent one of the most promising technologies in the strive towards a coal- and oil-free economy [11, 22, 23].

As schematically illustrated in Figure 1.1, fuel cells are composed of an ion- or proton-conducting material (electrolyte) that is sandwiched between two electrodes, an anode and a cathode. The conversion of chemical energy into electricity is based on the chemical reaction between hydrogen (H_2), contained in the fuel, and oxygen (O_2) to produce water (H_2O). Usually the fuel is supplied at the anode, and an oxidant is supplied at the cathode. The reaction on the anode generates electrons which can be accepted on the cathode, and that can move through an external electrical circuit. If the electrolyte is a solid oxide, the device is referred to as a solid oxide fuel cell (SOFC). In order to be used as electrolyte in a SOFC, the conductivity of the proton conducting material should effectively exceed $\approx 10^{-2}$ S·cm^{-1} [12]. This value is obtained

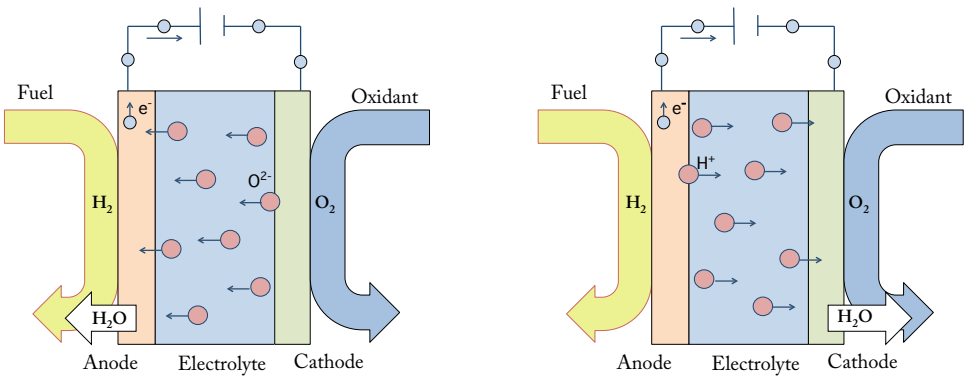

Figure 1.1: Schematic illustration of a fuel cell based on an oxide-ion conducting electrolyte (left) and one based on a proton conducting electrolyte (right).

from the ratio between the typical thickness, 15μm, and the maximum area specific resistivity allowed, 0.15 $\Omega{\cdot}\mathrm{cm}^2$, of electrolytes [12].

Currently, the most common SOFCs are based on oxide-ion conducting electrolytes of $ZrO_2{-}Y_2O_3$ solid solutions, known as yttria stabilized zirconia (YSZ), and operate above 500 °C [9]. However, such a high operation temperature brings some drawbacks, as, for instance, the fact that the start up time of the devices is long or that, because the cells have to endure high temperature, their life time is relatively short [24–26]. Prolonged exposure to high temperature may as well cause chemical interdiffusion between the materials of the electrolyte and the electrodes and mechanical stresses of the components due to thermal expansion [24, 25]. For these reasons, the operation at high temperature usually requires the use of expensive materials [24–27].

Lowering the operation temperature would potentially reduce these issues, and would in principle enable the application of SOFCs in portable and transportation devices [16, 26–29]. In this respect, SOFCs based on proton conducting oxide electrolytes have emerged as promising candidates for operation in the temperature range between 200 and 500 °C [27, 29–31]. However, the proton conductivity of the materials already available today is still below the target value of 10^{-2} $\mathrm{S}{\cdot}\mathrm{cm}^{-1}$. More specifically, the reported proton conductivity values can vary, depending on the oxide, from 10^{-7} and 10^{-2} $\mathrm{S}{\cdot}\mathrm{cm}^{-1}$ in the 200–500 °C temperature range, yet very few materials can reach conductivity close to 10^{-2} $\mathrm{S}{\cdot}\mathrm{cm}^{-1}$ below $T = 500$ °C [9, 11, 27, 29–31].

To overcome this obstacle, and to be able to design better materials, it

is imperative to understand which are the factors, *i.e.* materials structural, chemical and physical properties, that boost or hinder proton conductivity. In turn, this understanding requires the unraveling of the behavior of hydrogen atoms in solids on both a local and a macroscopic scale. This is a remarkably fascinating scientific problem, which has motivated an impressive amount of research regarding the coupling between local structure and dynamics and macroscopic or functional properties, such as ionic conductivity. As an example, in $BaZrO_3$-based proton conducting oxides a certain number of the Zr atoms are usually replaced by a dopant such as Y, In or Sc. Several studies have looked into the proton-dopant interaction, and it has been proposed that this interaction is of attractive nature and, as such, detrimental for proton mobility [32–37]. It has also been speculated that the vibrational dynamics of the protons and of the lattice (phonons) play an important role in proton conductivity [7,8,10,38–42]. Yet, due to the complexity of the problem, which involves several parameters such as chemical composition, long-range structural arrangement, local environments and vibrational dynamics, several challenges remain open. One of these challenges concerns the fact that the nature of the proton-dopant interaction is not completely clarified. In $BaZrO_3$-based oxides, depending on the type of dopant atom the conductivity of the materials can vary considerably, *e.g.* between 10^{-5} and 10^{-2} Scm^{-1} at $T = 300$ °C [30,31], but, the reason for this spread in conductivity is not understood. Similarly, the details of the coupling between vibrational dynamics and conductivity remain unclear.

Further, there is nowadays a growing interest in reducing the thickness of the electrolyte, below 1 μm, for application in miniaturized devices such as micro-SOFCs, where one uses thin films of proton conducting oxides [12, 28, 43–45]. Due to the intrinsic difference between a thin film and a powder sample, new challenges and research questions opens up. For instance, a problem hindering conductivity in powder samples is the presence of grain boundaries, which can be avoided in epitaxially grown, crystalline, films [46, 47]. Additionally, films may be strained and textured, which affects significantly the performance of the electrolyte [45–50]. From one side, new investigations are required in an effort to extend our current knowledge about bulk powder samples to thin films. On the other side, the possibility to prepare and manipulate thin films represents a valuable, yet not fully exploited, tool for the study of the fundamental properties of proton conducting oxides.

Another new exciting possibility to advance the understanding of hydrogen dynamics in perovskite materials has recently emerged with the discovery of the perovskite type oxyhydrides, $ATiO_{3-x}H_x$ (A = Ba, Sr, Ca) [51–53]. Per-

ovskite type oxyhydrides do not contain mobile protonic species (H^+) as proton conducting perovskites. Instead, the hydrogens in these oxides are of hydridic nature (H^-), and most likely mobile. However, several aspects regarding the plausible hydride ion dynamics and their interaction with the surrounding atoms are yet to be understood. In particular, a clear interpretation of how the local dynamics of the hydride ions depend on the concentration of hydride ions and oxygen vacancies, and on temperature, is lacking.

1.1 Overview and aim of the thesis

On the basis of the background given, this thesis focuses on investigations of local structure and dynamics in perovskite-type oxides, including both proton and hydride ion conducting materials, and is divided into three complementary research themes. The first research theme concerns the investigation and characterization of the local environments and vibrational spectra of hydrogen, in both proton and hydride ion conducting materials, *i.e.* acceptor doped $BaZrO_3$ and $BaTiO_{3-x}H_x$. The studies are based on the use of inelastic neutron scattering (INS) and IR spectroscopy, and computer simulations. The unifying aim is to obtain insight into the proton and hydride ion local coordination environments as a function of the type and amount of dopant atoms, the amount of hydrogen and the presence of oxygen vacancies. The materials of choice exhibit a "simple", cubic, structure, which makes them suitable as model compounds for the investigation of local structure and dynamics in perovskite materials.

The second research theme concerns the nature of the incorporation of protons in $BaZrO_3$-based proton conductors. Specifically, the aim of this part is to investigate the possible presence of an uneven proton distribution, and the work pays particular attention to the connection between the structural properties of the perovskite structure, proton concentration and conductivity. For this purpose, epitaxial thin films of In-doped $BaZrO_3$ were investigated. The choice of thin films is motivated by the fact that they are particularly suitable for depth profiling, since well-established techniques, as for instance reflectivity and nuclear reaction analysis, can be used on films. A relatively high In-doping level ($\approx 50\%$) was chosen because it leads to a high nominal concentration of protons after hydration, thus providing a good signal/contrast in the experiments.

The third and last research theme concerns the lattice vibrational dynamics in $BaZrO_3$-based oxides, and their role in the dynamics of protons. In

particular, the investigation focuses on the lattice vibrations in $BaZrO_3$ and Y-doped $BaZrO_3$ by means of Raman and resonance Raman spectroscopy. The main aim of the study is to investigate Raman spectra measured for different incident photon energy and identify potential resonance energies. Additionally, the study aims to assess and discuss the potential of resonance Raman spectroscopy for the study of proton conducting oxides, specifically thin film samples, and the coupling between lattice and proton dynamics. Lattice dynamic are often investigated by "standard" Raman spectroscopy, but the Raman signal is usually weak. Further, since visible light is used, the penetration depth is of the order of 400-700 nm, which may represent a problem when investigations thin films. Resonance Raman spectroscopy, based on the use of UV light, may potentially solve these issues, but, up to now, there are no reports on resonance Raman spectra of $BaZrO_3$ based materials.

Chapter 2

Proton and hydride-ion conducting perovskite oxides

2.1 Perovskite oxides: a short overview

[(a)] Perovskite type oxides own their name from the perovskite mineral $CaTiO_3$, but the name is nowadays commonly used to refer to the class of compounds with the general formula ABO_3. A is usually a large divalent cation, such as Ba^{2+} or Sr^{2+}, and B is usually a smaller tetravalent ion, as for instance Zr^{4+}, Ce^{4+} or Ti^{4+}. In the "ideal" cubic perovskite structure the A cations occupy the body centered positions and the BO_6 octahedra occupy the corners of a cube, as schematically illustrated in Figure 2.1. However, depending on the specific relative sizes of the A and B cations, the structural arrangement may deviate from the ideal cubic to *e.g.* tetragonal, hexagonal or orthorhombic structure.

Because the perovskite structure can accommodate very different cations, the materials belonging to the class of perovskite type oxides are characterized by a large variety of different behaviors. Some examples are $BaTiO_3$ (BTO), which shows piezoelectric and ferroelectric properties, $BaBiO_3$-$BaPbO_3$ solid solutions, which exhibit superconductive behavior, and $LaMnO_3$, which shows magnetoresistance. Additionally, properties can be affected, and sometime finely tuned, by cation substitution (doping) on the A or B sites. For instance, the ferroelectric properties of BTO can be tuned by exchanging some Ba^{2+} ions with Pb^{2+} or Sr^{2+}ions. As another example, an insulator to metal transition can be obtained in $SrTiO_3$ and BTO by partially substituting Ti^{4+} with Nb^{5+}.

[(a)] The main references for this section, unless otherwise indicated, are Refs [54, 55].

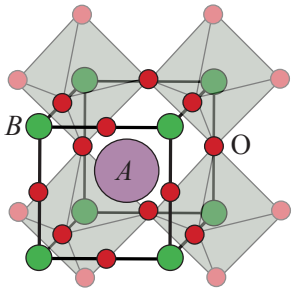

Figure 2.1: Schematic illustration of the cubic ABO_3 perovskite structure.

This versatility and property tuning can be utilized for different applications. Piezoelectric perovskite materials have the potential to be used in, for instance, sensors and actuators, whereas those showing dielectric properties may be used in capacitors, sensors or memory devices. Electrochromic perovskite oxides, *i.e.* materials that change color when an electric field is applied, have a wide application in so-called smart windows or mirrors. Perovskite oxides showing electronic conductivity can be used as anode or cathode materials in fuel cells, whereas, as already mentioned, those materials with proton conducting properties show potential as fuel cell electrolytes [24, 26, 56].

The materials of concern for this thesis are based on two perovskite oxides, barium zirconate ($BaZrO_3$, BZO) and barium titanate (BTO). BZO is a material with nearly perfect cubic perovskite structure, whereas BTO is a perovskite with a large A cation which goes through several structural changes as the temperature increases. At low temperature (<183 K) BTO shows a rhombohedral structure, whereas from 183 to 278 K and from 278 to 396 K it is characterized by an orthorhombic and tetragonal structure, respectively. Above 396 K, the material shows a cubic structure [55, 57].

2.2 Proton conducting perovskite oxides

Proton conduction in oxides was observed for the first time around the year 1960 [9, 10, 58] and the investigation of proton conducting perovskite oxides started few decades later (1980-1990) with the work from Iwahara and coworkers [30, 59–62]. These were, in particular, the first reports discussing the potential of acceptor doped $SrCeO_3$, $BaCeO_3$ and BZO. Barium cerate based materials exhibit better conductivity but are more likely to degrade with time

because of their tendency to react with CO_2 and water [63]. In contrast, acceptor doped BZO, where tetravalent Zr atoms are substituted by trivalent dopants, *e.g.* Ga, Sc, In, Gd or Y, are the materials that combine chemical stability with high proton conductivity in the 200–500 °C temperature range. They can reach conductivity values up to 10^{-3}–10^{-2} S·cm^{-1} [11, 29, 63, 64], but the use of one specific dopant instead of another one can determine a shift of several orders of magnitude of the maximum proton conductivity. For example, at $T = 300$ °C the maximum proton conductivity of doped BZO varies from 10^{-5} to 10^{-2} Scm^{-1}, where the doping with Ga results in the lowest conductivity and the doping with Y results in the highest [30,31,65,66].

Not surprisingly, these proton conductivity data illustrate that the mechanism involved during conduction must be strongly influenced by the structural properties of the material, both on a macroscopic and on a microscopic level. Nevertheless, measurements of proton conductivity alone cannot provide insight about the mechanism involved during the conduction process or about the local structure and dynamics. For this reason an increasing number of other experimental techniques, which are more suitable for the investigation of local structure and dynamics, have been employed. Among others, quasielastic neutron scattering (QENS) [32–34, 67–70], nuclear magnetic resonance (NMR) [35, 36, 71, 72], vibrational spectroscopy [70, 73–78], muon spectroscopy [34] and luminescence spectroscopy [79] have been used. Additionally, several investigations were also carried out by or in combination with computer simulations [35,37,71,73,80–91]. The results provided so far by means of these techniques, together with the most important questions still to be answered, are discussed in the following sections.

2.2.1 Incorporation of protons

Protons are not native members of the oxide structures, but can be incorporated by the reaction between oxygen vacancies present in the lattice and water vapor. This reaction, which is usually referred to as hydration, protonation or proton loading, leads to the formation of hydroxyl ions (OH^-) on oxygen sites. Oxides do not always contain oxygen vacancies, if not in very small concentration, but an oxygen deficient structure can be obtained, in a controlled way, by the introduction of impurity in the material. For ABO_3 oxides this is usually achieved by acceptor doping, a process which consists in the substitution of some of the B^{4+} cations with acceptors, *i.e.* cations of lower valency, specifically M^{3+} ions. In the specific case of BZO, acceptor doping leads to compounds of composition $BaZr_{1-x}M_xO_{3-x/2}$. Typical dopants for the Zr sites

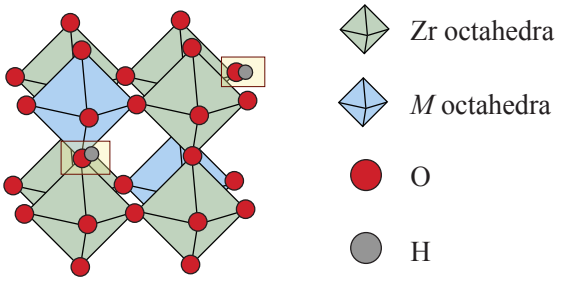

Figure 2.2: Schematic illustration of the cubic perovskite structure of hydrated, acceptor doped BZO, of general formula $BaZr_{1-x}M_xO_3H_x$. Ba atoms are omitted for clarity. The presence of hydroxyl groups (OH^-) is highlighted in the structure.

are Y^{3+}, In^{3+}, Sc^{3+}, Yb^{3+}, Ga^{3+} and Gd^{3+}.

Proton can be incorporated into the acceptor doped, oxygen deficient structure through hydration, which is often performed by exposing the materials to a humid atmosphere during heating. During this process the water molecules (H_2O) in the gaseous form may dissociate into hydroxyl groups (OH^-) and protons (H^+) on the surface of the sample, where the first ones may then fill the oxygen vacancies, and the second ones can bind to oxygen atoms of the lattice. The simultaneous diffusion of protons, from the surface towards the bulk of the material, and of oxygen vacancies, from the bulk towards the surface, allows new molecules to dissociate. More dissociation of water molecules on the surface leads to more protons in the bulk of the material, and this process can, theoretically, continue until when all the oxygen vacancies of the materials have been filled. This can be written as

$$BaZr_{1-x}M_xO_{3-x/2} + H_2O \Rightarrow BaZr_{1-x}M_xO_3H_x,$$

where the final situation is referred to as a full (complete) hydration of the material [Figure 2.2].

However, the protonation degree reported in the literature for hydrated acceptor doped BZO varies in a quite broad range, between 60% and 100% [31, 64, 65, 92–97], and, in a few reported cases, even hydration degrees higher than 100% have been observed [70, 97]. A low protonation degree is an indication of unfilled oxygen vacancies in the material. The presence of such unfilled oxygen vacancies or an excess of protons points toward the likelihood that the protons may distribute unevenly in the material. The effects of oxygen vacancies and of

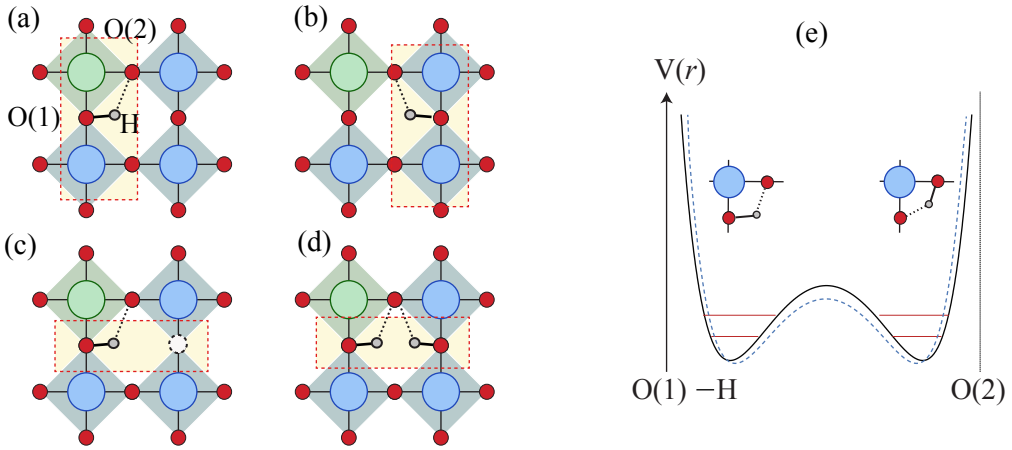

Figure 2.3: (a-d) 2-D sketch of different possible proton sites in the cubic structure of $BaZr_{1-x}M_xO_3H_x$, Green, blue and red spheres represent Zr, M and oxygen atoms. The presence of an oxygen vacancy is indicated with a white sphere in an oxygen site. (e) Sketch of the double-Morse type potential, V(r). Changes in the potential shape, as described in the text, are indicated by the blue dotted line. Red lines indicate the vibrational O-H stretch modes.

an uneven distribution of protons on key materials properties, such as proton conduction, are not known.

2.2.2 Local structure and proton sites

Protons in oxides are generally considered as protonic defects in a host structure. As illustrated in the example of Figure 2.3 (a), a proton form a covalent bonded to one oxygen atom, O(1), of the lattice, where the covalent bond H-O(1) is indicated by a continuous line. The proton can form, additionally, a hydrogen bond with a neighboring oxygen atom, O(2), indicated here as H··O(2) and with a dotted line in Figure 2.3 (a).

Due to the presence of several structural defects, such as dopant atoms, the protons can be located in different local environments, or proton sites, where each site can be defined by the chemical composition and structural arrangement around the proton. A proton can, for instance, be part of a hydroxyl group located between two different ions [Figure 2.3 (a)] or between two dopant atoms [Figure 2.3 (b)] or even close to an oxygen vacancy [Figure 2.3 (c)]. A proton may also be in the proximity of another proton [Figure 2.3 (d)], where the likelihood of this event is dependent on the proton density. Further, an

environment can be characterized by distortions with respect to the average, in this case cubic, structure. These distortions may be driven by the presence of defects in the structure, indicating a sort of "indirect", and even long range, proton-defect interaction.

A proton covalently bonded to an oxygen atom O(1) and forming a hydrogen bond with a second oxygen atom O(2), as described above, is occupying a minimum in a double-Morse type potential, as schematically illustrated in Figure 2.3(e). The shape of the potential can change from site to site, and it is strongly affected by the local structure, for instance by the O(1)-O(2) distance and the length of the covalent and the hydrogen bonds.

2.2.3 Dynamics

Proton diffusion

Protonic defects in oxides are able to migrate, or diffuse, through the lattice. On the short-length scale the diffusion of protons can be described by the so-called Grotthuss mechanism, *i.e.* the repetition of (i) a transfer of the protons between oxygen atoms and (ii) a reorientation of the O-H bonds [64, 98]. This mechanism is schematically illustrated in Figure 2.4, where the proton is initially bonded to an oxygen atom O(1) and forms a hydrogen bond with O(2). During the transfer from O(1) to O(2), Figure 2.4 (a), the proton forms a new H-O(2) covalent bond and a new O(1)··H hydrogen bond. When the O(1)··H bond breaks, the H-O(2) bond is free to rotate until a new hydrogen bond, to another oxygen atom of the perovskite lattice, is created [Figure 2.4 (b)]. According to this description, the short scale diffusion relies on an alternating formation and breaking of hydrogen bonds.

Note that the transfer involves the movement of the proton from one minimum of the double-Morse type potential, Figure 2.3 (e), to another, which requires the overcome of the energy barrier between the two proton sites. The rotation step requires instead the energy necessary to break the hydrogen bond. It has been longly debated which of the two elementary transport steps requires more energy, or, in other words, which process occurs with lower rate and therefore hinders the proton conductivity.

Nevertheless, at the present time there is not a clear answer to this question. Several studies have supported the theory that the reorientation is the fastest of the two steps [80–82, 99], but others have suggested that the two steps may have similar rates [38, 64], or even that the reorientation step may actually be the rate-limiting one [39, 86]. Not only may the "truth" depend on the specific

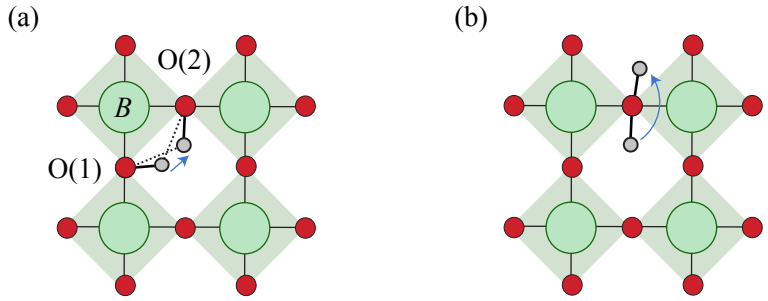

Figure 2.4: Schematic 2-D representations of a proton transfer (a) and a O-H bond reorientation (b) in a cubic ABO_3 perovskite structure.

system, but the results of simulations are strongly dependent on the simulation parameters and functional, and, from the experimental point of view, the results may vary depending on sample-to-sample differences. Additionally, for a specific proton site, the shape and hight of the potential barrier, together with the orientation and length of both covalent bonds and hydrogen bonds, are strongly influenced by the environment around the protons [37,73,83,100]. It follows that transfer and reorientation rates are likely to be site dependent, as strongly supported by recent QENS experiments [70, 101, 102].

O-H vibrational dynamics

Since protons are covalently bonded to the oxygen atoms of the perovskite lattice, they participate to the O-H vibrational modes, referred to as local vibrational modes since, unlike phonons, they do not propagate throughout the lattice. These modes may be divided into O-H bend, δ(OH), modes, also referred to as O-H wags or librations, and O-H stretch, ν(OH), modes, which are schematically illustrated in Figure 2.5.

Regarding acceptor doped BZO, ν(OH) modes are generally found at energies between 250 and 450 meV, whereas the δ(OH) modes are found at energies between, approximately, 100 and 150 meV.[(b)] IR spectroscopy measurements have revealed that the ν(OH) band is, for these materials, very broad and structured [64, 73, 78, 104], and similar observations were made, by means of neutron spectroscopy measurements, for the δ(OH) band [74]. As an example of this, Figure 2.6 (a) shows the IR spectra of 10In/BZO and 50In/BZO in the

[(b)] Experimental and calculated O-H vibrational frequencies in acceptor doped perovskite oxides can be found elsewhere [64, 73, 74, 83, 88, 92, 103, 104].

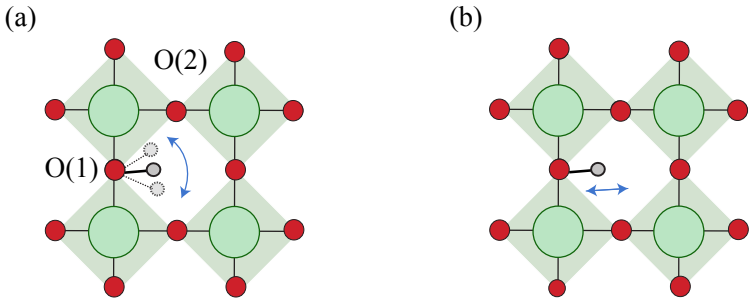

Figure 2.5: Schematic 2-D representations of (a) the δ(OH) mode and (b) the ν(OH) mode in a cubic perovskite structure. The arrows indicate the direction of the motion.

ν(OH) region. Additionally, it was shown that the δ(OH) band mirrors the ν(OH) band, which indicates that a high-energy ν(OH) modes correspond to low-energy δ(OH) modes, and *vice versa* [74].

The shape and size of the δ(OH) and ν(OH) bands suggest that they are the result of the overlapping of several different contributions, reflecting the co-existence of several unique local proton environments in the structure of the material, each characterized by a specific local arrangement around the proton and a different length (strength) of the hydrogen bond. The shortening (strengthening) of the hydrogen bond, in particular, causes the O-H stretch modes to shift towards lower energy (red-shift) and the wag modes to shift towards higher energy (blue shift) [38, 73, 74, 105, 106].

It has been suggested that the O-H vibrational dynamics are closely related to the proton transport and that both the transfer step and the reorientation step can be promoted by thermal or optical excitation. For instance, if the first O-H stretch vibrational level is populated, the proton effectively needs less energy to cross the energy barrier between the two minima of the double-Morse type potentia [Figure 2.3 (e)], thus vibrational dynamics may promote the transfer step [7, 8, 69, 73]. The role of the O-H vibrational modes, specifically ν(O-H) modes, in hydrogen dynamics has been investigated by Sphar and coworkers [7,8] using a picosecond transient bleaching technique combined with IR absorption spectroscopy. As an example, they studied hydrogen dynamics in Rutile TiO_2 containing a small amount of "as-grown" hydrogen, where the H atoms are part of hydroxyl groups (OH^-). One of the keys results of this work is that the excitation of the ν(O-H) mode couples a δ(O-H)-assisted proton transfer (jump).

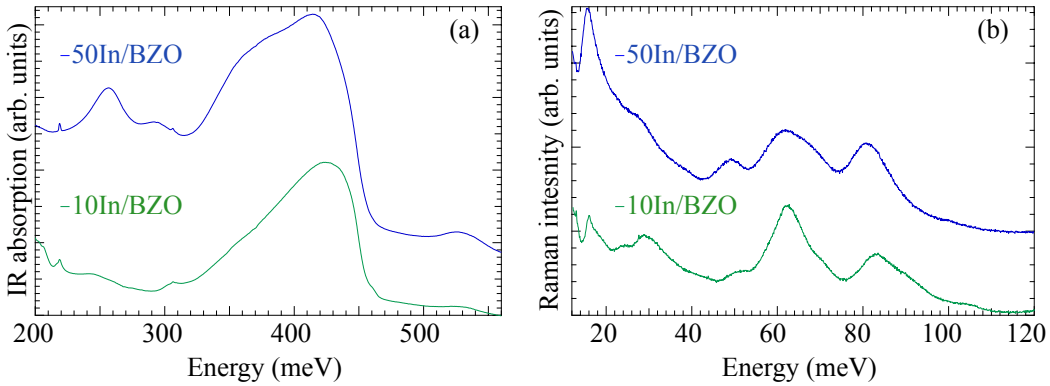

Figure 2.6: (a) IR absorbance spectra over the ν(OH) region and (b) Raman spectra over the lattice modes region for hydrated 10In/BZO and 50In/BZO [see paper II]. The spectra have been vertically separated for clarity.

These findings strongly suggests that both vibrational modes play a crucial role in the diffusion of protons. Therefore, it is likely that a similar process occurs in other materials, such as acceptor doped BZO, *i.e.* that vibrational dynamics can influence the transfer and reorientation rates. It is important to notice that, conversely to acceptor doped BZO, in TiO_2 the O-H stretch band is a sharp peak at 407 meV. This means that the vibrational dynamics in acceptor doped BZO are site dependent, which therefore reflects on the transport steps.

Lattice dynamics

The lattice vibrations, or phonons, of BZO based oxides are found below 100 meV in the vibrational spectra, *i.e.* at lower energies with respect to the O-H vibrational dynamics [75, 76, 78, 107]. Figure 2.6 (b) shows, as an example, the Raman spectra of 10In/BZO and 50In/BZO. Bands below ≈25 meV are generally assigned to deformational motions of Ba-[(Zr/M)O_6] units, whereas the bands above ≈25 meV are related to vibrational modes of oxygen atoms [75, 76].

Note that a perfectly cubic perovskite should have only four optical, triply degenerate, phonons, three of which are IR active, and none of which is Raman active. Any impurity or deformation of the cubic structure may, however, lead to a change in the structural symmetry and hence to the activation of Raman modes, the appearance of new contributions to the spectrum or the broadening of the spectral features [75,107]. According to diffraction data, acceptor doped

BZO possesses an average cubic structure [78, 93–95, 100, 108–110]. The presence of features in the Raman spectra of these materials suggests, therefore, that the cubic symmetry is locally distorted [75, 76]. This is not surprising, since the materials contain dopant atoms, protonic defects and perhaps unfilled oxygen vacancies, which can all be considered as impurities and can lead to local structural distortions.

Since the rate of proton transfer may strongly depend on the distance between the two neighboring oxygen atoms, vibrational dynamics involving the oxygen atoms may be of importance for the proton transfer rate. More specifically, it has been longly hypothesized that proton transfer is possible only when the oxygen-oxygen distance get, momentarily, small enough for the proton to "jump" from one oxygen to another [10]. There is nowadays a quite wide consent about the fact that, similarly to O-H vibrational modes, lattice vibrations, and in particular those involving displacements of oxygen atoms, play an important role in the proton transfer process [10,38–41]. However, the details of this plausible"phonon assistance" are not clear.

2.2.4 The role of local coordination

Dopant atoms and proton-dopant association

Although it is well known that the introduction of dopant atoms in the perovskite lattice affects the local structure of the material [73–76,76,89,96], there have been several hypothesis about which properties of the dopant are of relevance in the determination of the material diffusion properties. Among others, the size, or ionic radii [31, 37, 110] and the electronic structure [31, 64, 88, 96, 111, 112] have been discussed in detail. Yet, the connection between these properties and the proton conductivity is still not fully clarified. On the contrary, investigation of proton local dynamics showed no relevant dependence on the type of dopant (Y, In or Sc) [70, 101, 113].

The interaction between a proton and the dopant atoms has been widely investigated in scenarios where one can consider only one single proton interacting with one single dopant atom, which is comparable to a low doping regime, *i.e.* a doping level below 20% [32–35]. In this regime, dopants are often described as trapping centers, indicating that the proton is attracted to the dopant and, during diffusion, tends to spend more time close to the dopant [32–35]. This view was initially introduced, few decades ago, by Hempelmann and coworkers, and supported by QENS results on $SrCe_{0.95}Yb_{0.05}H_{0.02}O_{2.985}$ [32, 33] and muon spin relaxation study on Sc-doped $SrZrO_3$ [34]. QENS results, in particular, indicated the presence of two dynamical processes, one

slower than the other. The slowest dynamics were associated to proton sites close to "trapping-centers", *i.e.* the dopant atoms, whereas the fastest were assigned to proton sites in "trap-free" regions.

More recently, Yamazaki and coworkers investigated proton trapping in Y-doped BZO by means of NMR measurements combined with conductivity measurements [35]. The results from this study supported the view of dopant atoms as trapping center, and suggested that while at room temperature the majority of the protons are trapped, increasing the temperature they can escape the trapping sites. The authors also proposed that trapping sites in Y-doped BZO are characterized by stronger hydrogen bond. Proton trapping was also reported for Sc-doped BZO in recent studies based on a combination of NMR and computer simulations [36, 71]. Further support to this proton trapping scenario were provided by luminescence spectroscopy [79] and computer simulations [37, 84–87, 114].

The "typical" proton-trapping scenario does not take into account the presence of dopant pairs or groups of neighboring dopants. In this respect, it is important to consider that even if a proton is associated with a dopant, it can still undergo to local motion, both jump and reorientation, around the dopant [35]. This would suggest that in a high-doping scenario a proton could move from trapping center to trapping center without really escaping from them. Recent computational results suggest that the trapping effect seems to be enhanced when two or three dopants (Y) are close to each other [91]. Nevertheless, the presence of a network of dopant atoms creates a sort of preferential conduction pathway, where the protons can move without de-trapping [91]. According to this study, the trapping effect would be moderate by the presence of a high density of dopant atoms. However, conductivity measurements have shown that the proton conductivity in $BaZr_{1-x}Y_xO_3H_x$, with $x > 0.2$, decreases with increasing doping level. This was interpreted as the fact that, above $x \approx 0.2$, the increase of the density of dopant atoms somehow enhances the trapping effect [97].

It has also been proposed that, rather than as well-localized trapping centers, the dopant-proton interaction may occur in a more delocalized manner [40, 64, 67]. Giannici *et al.* suggested, supported by X-ray absorption spectroscopy, that the different proton conductivity values associated to different dopants in BZO relates with the disorder that the dopants introduce in the host lattice, and its effect on the electronic structure [96, 111, 112]. In their view, those dopants which give rise to the highest proton conductivity, *e.g.* Y^{3+}, are the ones which introduce high local disorder and have low solubility in the host matrix. Accordingly, they proposed that the In^{3+} cation mimics

the doped atom (Zr^{4+}), while the Y^{3+} cation acts as a rigid inclusion in the host lattice.

Proton-proton interaction

The protons themselves can be considered as charged defects, and the insertion of charged defects influences both the short- and long-range structure of the perovskite [83, 115], as it is shown, for example, by the expansion of the unit cell volume upon hydration [93, 97, 100, 108]. The presence of protonic defects can distort the local structure, for instance, by pulling oxygen atoms close together [37]. Hence, the presence of protons may affect the local environment of other protons, indicating an indirect type of interaction. And yet, only few works have investigated the proton-proton interaction, and possible effects on proton trapping and proton diffusion, in a scenario with multiple protons.

Gomez and coworkers presented one of the few works where two protons are considered [90]. In their computational study on Y-doped BZO they suggested that the presence of several protons actively reduces the trapping effect. Their results also indicate that the protons tend to pair, in agreement with previous results from Bork *et al.* [116] on $SrTiO_3$. According to these works, the effect of one proton on another one is mediated by local lattice distortions, *i.e.* the presence of one proton distorts its surrounding environment and therefore affects the local environment of any proton in the vicinity. The interaction may be, therefore, described as indirect, in opposition to a direct, for example electromagnetic, interaction. Interestingly, the presence of an extended distortion domain has been suggested as the origin of an increased hydrogen bond strength in such multiple-proton scenario.

Additional insights into the topic are given by Buannic and coworkers and their work on Sc-doped BZO [36, 71]. They considered different scenarios of two protons in the proximity of each other [71]. Interestingly, configurations where both protons are "trapped", *i.e.* are situated close to dopant atoms, are not the most energetically stable ones. The most energetically favorable scenario appeared instead to be the one where one proton is close to a dopant atom whereas the other is close to a Zr atom. Further, one of the most stable configurations was found to be the one where the same oxygen atom accepts both the covalent and the hydrogen bond, which would confirm the presence of a strong, but indirect, interaction between protons.

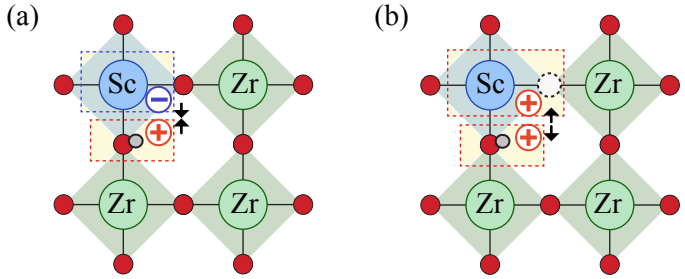

Figure 2.7: Schematic view of the interaction between protonic defect and acceptor (a) and between protonic defect, acceptor and oxygen vacancy, redrawn from ref. [72].

Oxygen vacancies and other defects

The presence of dopant atoms and protons is not the only factor that determines the local structure, as other defects may as well contribute. As an example, oxygen vacancies are well known structural defects which interact strongly with the protons in proton conducting oxides [115, 117, 118]. Oxygen vacancies can be described as a positively charged defect, with charge +2. Computational results have suggested that the the presence of an oxygen vacancy causes local lattice contraction, in particular due to the attraction between the positively charged defect and the negatively charged oxygen ions of the lattice [115, 117, 118].

In a recent NMR study of Sc-doped BZO Oikawa and coworkers [72] suggested that the oxygen vacancies cluster close to the Sc-atoms, and their presence mitigate or eliminate the trapping effect of the dopant. Using a relatively simplified description, in acceptor doped $BaZrO_3$ the acceptor, *e.g.* Sc, has a negative net charge, and can therefore attract and trap a proton, which is characterized by a positive charge, as schematically illustrate in Figure 2.7 (a). It is suggested that the association of a dopant with an oxygen vacancy also results in a positively charged defect, as schematically illustrated in Figure 2.7 (b). The authors propose that the electrostatic repulsion between the proton and the oxygen vacancy, of positive charge, effectively cancels out the negative charge of the Sc-dopant. This suggests that proton-dopant attraction may be significantly reduced in a system containing oxygen vacancies. Similar claims have been done also for other dopants, even though the presence of oxygen vacancies do not affect each material in the same way [119].

It is worth to mention that, despite they are not further discussed in this thesis, there are other factors of practical importance for structure and proton

conductivity in acceptor doped perovskite oxides, such as the presence of grain boundaries [63, 64, 120–123] and *A*-site non-stoichiometry [124, 125]. Grain boundaries are characterized, with respect to the bulk of the grain, by a high resistivity, which is known to lower the overall proton conductivity of the material [63,64,120,123]. The discussion about the origin of the grain boundary resistance is beyond the aim of this thesis, yet, it is important to note that regions at and near grain boundaries are different from the bulk of a grain [120,121,126,127]. Hence, proton sites at the grain boundaries and bulk proton sites are probably not alike, and this needs to be taken into account in the investigation of the nature and distribution of proton sites in these materials. Considering *A*-site non-stoichiometry, Ba deficiency is known to be detrimental for proton conductivity in Y-doped BZO [124, 125].

2.3 Hydride-ion conducting perovskite oxides

Perovskite oxyhydrides, of general formula $A\mathrm{TiO}_{3-x}\mathrm{H}_x$ (A =Ba, Sr, Ca and $x < 0.6$), are a novel class of oxyhydrides which have emerged as interesting materials towards mixed electronic-ionic conductors with potential application in energy storage and conversion [51–53]. Conversely to proton conducting oxides, where the hydrogen atoms are part of hydroxyl groups (OH^-), in oxyhydrides the hydrogen atoms are present as hydride ions (H^-) on oxygen sites, *i.e.* they are situated in the lattice.

Until less than 10 years ago the presence of hydridic hydrogen have been reported in relatively few materials other than perovskite oxyhydrides, such as LaHO [128], $\mathrm{Zr_5Al_3O_{0.5}H_{4.8}}$ [129], $\mathrm{Ba_{21}Ge_2O_5H_{24}}$ [130], $\mathrm{Ba_3AlO_4H}$ [131], $\mathrm{Sr_3Co_2O_{4.33}H_{0.84}}$ [132], $12\mathrm{CaO}{\cdot}7\mathrm{Al_2O_3}$:H [133]. One of the main reason for such limited number of reports is that for a long time these materials have been rather difficult to synthesize. The obtained oxyhydrides were often unstable and the content of hydride ions difficult to control. In 2002 it was reported, for the first time, the synthesis of $\mathrm{LaSrCoO_3H_{0.7}}$ [134,135] *via* a simpler approach, known as topochemical reaction. These exciting developments opened up to the possibility to expand the class of oxyhydride materials.

2.3.1 Synthesis, structure and electronic properties

On the basis of the approach proposed in 2002, in 2012 Kobayashi and coworkers proposed to synthesize perovskite oxyhydride $A\mathrm{TiO}_{3-x}\mathrm{H}_x$ *via* the topochemical reaction between $A\mathrm{TiO_3}$ and the metal hydride $\mathrm{CaH_2}$ [51]. During the isotopic reaction the metal hydride reduces the Ti^{4+} ions and creates oxygen

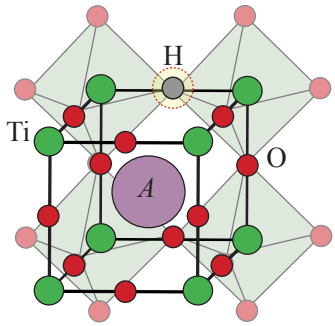

Figure 2.8: Schematic illustration of the cubic perovskite structure of $A\mathrm{TiO}_{3-x}\mathrm{H}_x$. The presence of an hydride ion, located on an oxygen site, is highlighted in the structure.

vacancies in $A\mathrm{TiO}_3$, which are filled by the hydride ion, therefore creating the oxyhydride. This can be seen, hence, as the substitution of hydride ions for oxygen atoms of the $A\mathrm{TiO}_3$ lattice, as illustrated in Figure 2.8. The formation of hydride species on oxygen sites relies on the fact that titanium has more than one oxidation state. More specifically, in the oxyhydride phase the O^{2-} and H^- ions form the octahedral environment around Ti atoms, which makes the Ti atoms exist in a mixed IV/III oxidation state [51]. An important properties of $A\mathrm{TiO}_{3-x}\mathrm{H}_x$ oxyhydrade is that they are stable at room temperature and up to ≈ 400 °C. Above this temperature the hydrogen are released, which is a strong indication of hydride ion diffusion through the perovskite structure [53].

Kobayashi and coworkers managed, using the topochemical approach as described above, to synthesize the perovskite oxyhydrade $\mathrm{BaTiO}_{3-x}\mathrm{H}_x$ [51]. The work motivated further effort in the synthesis and characterization of perovskite oxyhydride $A\mathrm{TiO}_{3-x}\mathrm{H}_x$ [52]. In a recent work, Nedumkandathil and coworkers [136] showed that $\mathrm{BaTiO}_{3-x}\mathrm{H}_x$ samples can be obtained by using different metal hydrides other than CaH_2 to reduce BaTiO_3, such as NaBH_4, NaH, MgH_2 and NaAlH_4.

Among other oxyhydrides, $\mathrm{BaTiO}_{3-x}\mathrm{H}_x$ is the material exhibiting the highest amount of hydride ions obtained using this approach, with a concentration up to $x \approx 0.6$. Interestingly, in BTO-based materials the change of the oxidation state of the Ti ions causes an expansion of the structure with respect to the BTO structure, and, as a result, the material is, differently from BTO, cubic at all temperatures [57]. The introduction of the hydride ions influences also other properties of the material. For instance, introduction of hydride ions can be

seen as a donor doping of the material, since the insertion of H^- contributes to electronic (n-type) conductivity [137–139]. Conductivity measurements have confirmed that $BaTiO_{3-x}H_x$ is, indeed, electronically conductive [51, 137].

The presence of the hydride ions in the perovskite structure also influences the color of the material, which goes from white for $BaTiO_3$ to blue for $BaTiO_{3-x}H_x$. This color change has been investigated by Schrader *et al*, who suggested that the phenomena is related to a hopping process of polarons [140]. A polaron is an electron, in this case the one donated by the hydrogen, which is localized at a specific site, here the Ti site. However, the extra electron could, instead of creating a polaron, be delocalized within the electronic band [57]. Despite electronic conductivity and materials color change are both related to the presence of an extra electron in the structure, it is still debated in literature whether the extra electron localized or delocalized [137, 140].

2.3.2 Dynamics

Hydride ion diffusion

Since hydride ions are expected to be mobile in the oxide host, it has been discussed which is the mechanism that can describe their diffusion through the perovskite structure. Investigation of other type of oxyhydrides have shown that the diffusion can be enhanced by introducing oxygen vacancies in the materials [141–143]. This was the case for $La_{1-x}Sr_{1+x}LiH_{2-x}O_2$ [141], where pure H^- conductivity can be observed and can be boosted by the introduction of oxygen vacancies. Investigations on $EuTiO_{2.82}H_{0.18}$ [143] and $SrTiO_3$ [142] show that the presence of oxygen vacancies allows anionic exchanges, hence, oxygen vacancies must somehow promote the mobility of anionic species.

In $BaTiO_{3-x}H_x$ the mobility of the hydride ions was demonstrated by hydrogen / deuterium exchange [51, 144], and two main diffusion mechanism has been proposed so far. The first mechanisms is a diffusion aided by the presence of oxygen vacancies. In the presence of a neighboring vacancy the ion may "jump" from its position and occupy the vacant site, as illustrated in Figure 2.9 (a-b). This diffusion mechanism may require, therefore, a complementary diffusion of oxygen vacancies and oxide ions. Indeed, results from hydrogen / deuterium exchange measurements [144] suggest that for a low content of hydride ions ($x < 0.4$) the H^- diffusion requires the diffusion of oxygen ions. However, for a higher hydrogen content the H^- ions seem to form a preferential conduction pathway, independent on the oxygen diffusion.

Recent QENS results [145] have shown that in the presence of enough oxygen vacancies the diffusion is likely independent on the counter diffusion of

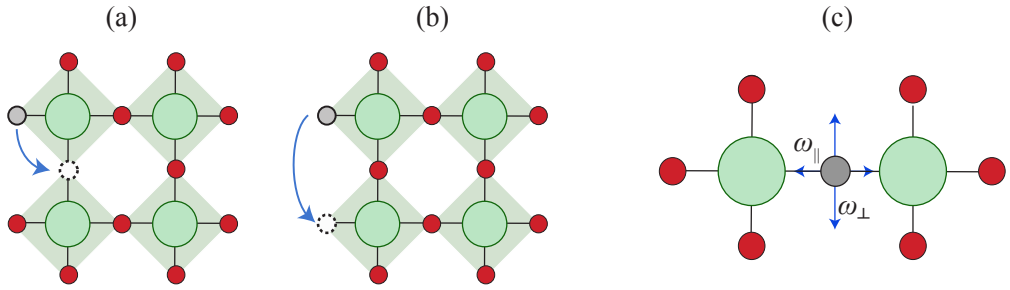

Figure 2.9: (a-b) Schematic representation of possible hydride ion vacancy assisted diffusion events in the $BaTiO_{3-x}H_x$ structure, characterized by the "jump" of the ion into neighboring, vacant, oxygen sites and (c) 2-D sketch of the $\omega_{\parallel}$ and $\omega_{\perp}$ vibrational modes of the hydride ion in $BaTiO_{3-x}H_x$. The arrows indicate the direction of the motions.

oxygen ions. This suggests a scenario where oxygen vacancies form a percolating pathways in the perovskite lattice, and the diffusion occur through jumps to neighboring oxygen vacancy sites. Further, computational results from Tang and coworkers [144] indicate that diffusion of hydride ions may occur through jumps between nearest neighboring sites (Figure 2.9 (a)) as well as next-nearest neighboring sites (Figure 2.9 (a-b)). In this respect, QENS measurements suggest that at low temperature (≈250 K) the jumps are more likely between nearest neighboring sites, whereas at higher temperature (≈400 K) hydride ion may jump between next-nearest neighboring oxygen vacancies. The second possible diffusion mechanism, alternative to this vacancy-assisted diffusion, is that the hydride ions first become protons which then diffuse interstitially [51, 137–139, 146]. The results discussed so far do not completely clarify whether, during diffusion, the hydride ions maintain their negative charge. However, the presence of protonic states is not supported by any experimental data reported so far.

Vibrational dynamics

Because of the different local coordination of protonic and hydridic species, the vibrational signature of the hydride ions in a perovskite oxyhydride is quite different from the one of protons in the proton conducting analogue. A systematic study of the vibrational spectra would give important insight about the local coordination of hydride ions and its role in the materials functional properties.For $BaTiO_{3-x}H_x$, where the hydride ions form Ti-H-Ti bonding,

the hydrogen atoms participate in the Ti-H vibrations. These consist of three vibrational modes, one, $\omega_{\parallel}$, along the Ti-H-Ti bond and two, degenerate, $\omega_{\perp}$, perpendicular to this bond direction, as schematically shown in Figure 2.9 (c).

Calculations have suggested that the Ti-H vibrational modes are characterized by vibrational energies between 100 and 130 meV [137]. However, these results did not distinguish between the presence of a polaron or an extra electron in the bandstate. In this context, a combined study of experimental and calculated vibrational spectra could be the key to discriminate the nature, localized or delocalized, of the extra electrons donated by the hydrogen atoms.

Chapter 3

Methodology

3.1 Neutron scattering: a brief introduction

Neutron scattering is an extremely powerful and versatile experimental method. This section aims to illustrate the basic principles of neutron scattering,[a] whereas the fundamentals of the specific techniques used in this thesis, inelastic neutron scattering (INS) and neutron reflectivity (NR), are discussed in the following sections.

In a neutron scattering experiment a sample is irradiated with neutrons, which are sub atomic particles displaying a wave-particle duality and that can exchange both energy and momentum upon scattering on the sample. The properties of the sample can be studied by investigating how the neutrons are scattered from the sample, *i.e.* by investigating the exchanged energy and momentum. A neutron is electrically neutral, and the neutron-matter interaction occurs *via* scattering on the atomic nuclei, mediated by the nuclear force. A neutron can also interact magnetically with matter, due to its magnetic spin, but this interaction can be neglected in the case of non-magnetic materials, as the ones studied here. The strength of the neutron-nucleus interaction is described by the scattering cross section σ or the scattering length b, where $\sigma = 4\pi b^2$ is expressed in barns (1 barn = 10^{-24} cm^2).

An interesting aspect of neutron scattering is that σ does not show any systematic dependence on the atomic number, which instead is the case for probes such as X-ray radiation. This means that neutrons are more sensible to the presence of some specific (light) atomic species which may be, instead,

[a] An extensive treatment of the principles of neutron scattering and neutron scattering based techniques can be found in Ref. [147–149], which are the main references for this section.

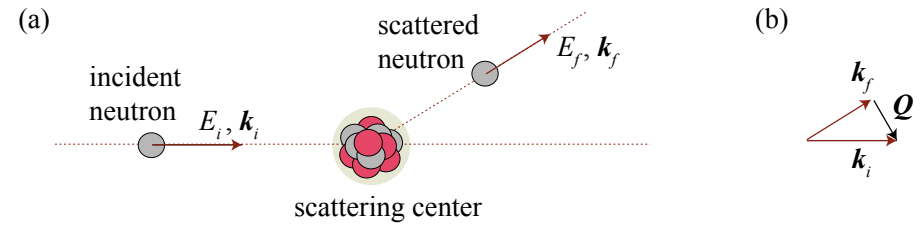

Figure 3.1: Schematic illustration of the neutron scattering process (a), as described in the text, where (b) shows the transferred momentum $\boldsymbol{Q}$ obtained as $\boldsymbol{k}_i - \boldsymbol{k}_f$.

difficult to detect with X-rays. This is the case of hydrogen atoms, as it will be further discussed. Due to their electrical neutrality and generally weak interaction with matter, neutrons are usually considered a not-perturbative and highly penetrating probe. It is worth to mention, before moving forward, that a sample can both scatter and absorb neutrons.

A sketch of a neutron-nucleus scattering event is depicted in Figure 3.1. The energy and momentum exchanged are determined by the initial (i) and final (f) states of the neutron, *i.e.* before and after the scattering event. These two states are described by the initial and final momentum of the neutron, $\boldsymbol{k}_i$ and $\boldsymbol{k}_f$,[(b)] and by its initial and final energy

$$E_i = \frac{\hbar}{m_N} k_i^2, \quad E_f = \frac{\hbar}{m_N} k_f^2,$$

where m_N is the mass of a neutron. The energy and momentum transferred from the neutron to the sample are $\hbar\omega = E_i - E_f$ and $\boldsymbol{Q} = \boldsymbol{k}_i - \boldsymbol{k}_f$, respectively. When no energy is exchanged, *i.e.* $\hbar\omega = 0$, the scattering is referred to as elastic, otherwise the scattering is referred to as inelastic.

During a neutron scattering experiment, the measured quantity is usually the intensity of the scattering as a function of ω and Q, *i.e.* $I(Q, \omega)$. This intensity is proportional to the double differential cross section $d^2\sigma/dE_f d\Omega_f$, *i.e.* the number of scattered neutrons in the solid angle $d\Omega$ and having final energy in the interval $E_f \pm dE_f$, divided by the incident neutron flux, conventionally

[(b)] Bold symbols, such as $\boldsymbol{k}_i$, are used in this thesis to identify vectors. The norm of a vector $\boldsymbol{k}$ is simply indicated by $k = |\boldsymbol{k}|$.

expressed as

$$\frac{d^2\sigma}{dE_f d\Omega_f} = \frac{N}{4\pi\hbar}\left[\sigma_{\text{coh}} S_{\text{coh}}(\boldsymbol{Q},\omega) + \sigma_{\text{inc}} S_{\text{inc}}(\boldsymbol{Q},\omega)\right]. \tag{3.1}$$

Here

$$S_{\text{coh}}(\boldsymbol{Q},\omega) = \frac{1}{2N\pi\hbar}\sum_{i,j(i\neq j)}^{N}\int dt \langle e^{-i\boldsymbol{Q}\cdot\boldsymbol{r}_i(0)} e^{i\boldsymbol{Q}\cdot\boldsymbol{r}_j(t)}\rangle e^{-i\omega t} \tag{3.2}$$

$$S_{\text{inc}}(\boldsymbol{Q},\omega) = \frac{1}{2N\pi\hbar}\sum_{i} N\int dt \langle e^{-i\boldsymbol{Q}\cdot\boldsymbol{r}_i(0)} e^{i\boldsymbol{Q}\cdot\boldsymbol{r}_i(t)}\rangle e^{-i\omega t}, \tag{3.3}$$

where i and j label the N different scattering nuclei in the sample, $\boldsymbol{r}_i(t)$ is the time dependent atomic position of the nucleus i and $\langle\ \ \rangle$ indicates a thermal average. The quantity σ_{coh} and σ_{inc} are referred to as the coherent and incoherent scattering cross sections, and $S_{\text{coh}}(\boldsymbol{Q},\omega)$ and $S_{\text{inc}}(\boldsymbol{Q},\omega)$ are the coherent and incoherent dynamic structure factors.

The coherent part of the scattering intensity depends on the correlation, at different times, between the positions of two different nuclei. The incoherent part instead depends on the correlation between the positions of the same nucleus at different times. Coherent scattering contains information about the structure (elastic case), as in neutron diffraction or neutron reflectivity, and about collective motions of atoms (inelastic case). Incoherent scattering can, instead, probe the properties of individual atoms, such as hydrogen self-dynamics in acceptor doped $BaZrO_3$ or $BaTiO_{3-x}H_x$. Note that hydrogen has a particularly large incoherent neutron scattering cross section, see Table 3.1, which makes neutron scattering notably suitable for the study of proton incoherent dynamics, such as local dynamics (vibrations).

3.2 Vibrational spectroscopy

Atoms in materials are not still, rather they oscillate (vibrate) around their equilibrium positions. For each specific system the collection of all its characteristic vibrations is unique, a sort of fingerprint that can be used to identify compounds. Vibrational spectroscopy techniques probe the vibrational dynamics of atoms in a system and provide access to its vibrational spectrum, where characteristic vibrations are manifested as bands. Each vibrational band is characterized by its frequency, which depends on the type of atoms involved

Table 3.1: Coherent neutron scattering lengths, b_{coh}, and coherent, incoherent and total neutron scattering cross sections, σ_{coh}, σ_{inc} and σ_{tot}, of hydrogen atoms and other atomic elements of relevance for this thesis, taken from Ref. [150]. The symbols H and D stand for the two isotopes of hydrogen, ^{1}H and ^{2}H (deuterium), respectively.

Element	b_{coh} (fm)	σ_{coh} (barn)	σ_{inc} (barn)	σ_{tot} (barn)
H	-3.7390	1.7583	80.27	82.03
D	6.671	5.592	2.05	7.64
O	5.803	4.232	$8 \cdot 10^{-4}$	4.232
Sc	12.29	19.0	4.5	23.5
Ti	-3.438	1.485	2.87	4.35
Zr	7.16	6.44	0.02	6.46
In	4.065	2.08	0.54	2.62
Ba	5.07	3.23	0.15	3.38

in the vibration, their mutual chemical bonds and their geometrical arrangement. The intensity and shape of a band are instead defined by the number of vibrating species, the local structural arrangement of and around them and how well defined the vibration is.

A vibrational spectrum contains, therefore, information about the type of atoms and their structural arrangement in a material, but also about the presence and the nature of structural distortions, defects and different local configurations. One should note that the intensity and shape of a band may also depend on the nature of the probe, *e.g.* IR light or neutrons.

Vibrational spectroscopy techniques rely on the excitation (or de-excitation) of vibrational states, achieved either by the absorption of a photon at the energy of the vibration, as in IR spectroscopy, or by inelastic scattering, as in Raman and INS spectroscopy, where the exchanged energies correspond to vibrational energies. In both IR and Raman spectroscopy light is used to excite the vibrational states, and both rely on (different) selection rules, meaning that some modes may be IR and/or Raman silent (inactive). In INS, which is based instead on the use of neutrons, the intensity is proportional to the population of the vibrational species present in the sample and all vibrations are active, and therefore, in principle, measurable. Further, due to the differences between photons and neutrons, IR and Raman are limited to the observation of vibrational modes at the Brillouin zone centre, whereas INS is not.

3.2.1 Inelastic neutron scattering

This section is dedicated to the discussion of INS in the specific case of vibrational, incoherent, dynamics of hydrogen in powder samples, and the following description is developed in the framework of the incoherent approximation.[c] The INS intensity is calculated assuming that it results solely from hydrogen dynamics and treating all the scattering as incoherent but using the total scattering cross section [149], *i.e.*

$$I(\boldsymbol{Q},\omega) \propto \left.\frac{d^2\sigma}{dE_f d\Omega_f}\right|_{\mathrm{H}} = \frac{N}{4\pi\hbar}\sigma_{\mathrm{H,tot}} S_{inc}(\boldsymbol{Q},\omega)_{\mathrm{H}} \tag{3.4a}$$

$$\Rightarrow I(\boldsymbol{Q},\omega) = \sum_l I(\boldsymbol{Q},\omega)_l \propto \sum_l \int dt \langle e^{-i\boldsymbol{Q}\cdot\boldsymbol{r}_l(0)} e^{i\boldsymbol{Q}\cdot\boldsymbol{r}_l(t)}\rangle e^{-i\omega t}. \tag{3.4b}$$

Here l labels the different hydrogen atoms and $I(\boldsymbol{Q},\omega)_l$ is the contribution of the atom l to the total intensity.

For a specific hydrogen atom (l =H) in the vibrational mode ν, of energy ω_ν, it can be shown that

$$I(\boldsymbol{Q},\omega_\nu)^{(n)}_{\mathrm{H}} \propto \frac{\left(\boldsymbol{Q}\cdot\boldsymbol{u}_{\mathrm{H},\nu}\right)^{2n}}{n!} e^{-\left(\boldsymbol{Q}\cdot\sum_\nu \boldsymbol{u}_{\mathrm{H},\nu}\right)^2}, \tag{3.5}$$

where $n = 1$ indicates fundamental modes, $n = 2$ their first overtones, $n = 3$ their second overtones, and so forth. The symbol $\boldsymbol{u}_{\mathrm{H},\nu}$ refers to the displacement vector of the hydrogen atom along the direction of the vibration, and the sum in the exponential term runs over all the vibrational modes of the hydrogen atom, both internal and external.

The separation between internal and external modes is customary of molecular crystals, where one can distinguish between intramolecular, localized, modes and intermolecular, delocalized, modes. Internal (intramolecular) and external (intermolecular) modes are effectively decoupled from each other. In the systems investigated in this thesis the vibrational dynamics of hydrogenous species, *i.e.* the δ(O-H), ν(O-H) and Ti-H vibrational modes, can be all considered localized and decoupled from the lattice modes. One can therefore draw an analogy to molecular crystals and use the terms internal and external modes to refer to the highly localized vibrational modes of hydrogenous

[c] The complete derivation of the following results can be found in Ref. [149] and is based on the assumptions that (i) all modes are dynamically decoupled, (ii) the scattering can be described as completely incoherent and (iii) $2k_BT/\hbar\omega << 1$. For a more general derivation the reader may consult Refs. [147, 148].

species, mentioned above, and the phonon modes, respectively. Note that the decoupling is, here, the result of the large difference in mass between hydrogen atoms and the other atoms of the lattice.

For a powder sample, as the ones investigated in this thesis, the scattering intensity is comparable with the average of the dynamic structure factor taken with respect to all the possible directions in space, leading to an intensity $I(Q,\omega_\nu)^{(n)}_{\mathrm{H}}$ depending only on the scalar quantity Q. This can be written as

$$I(Q,\omega_\nu)^{(n)}_{\mathrm{H}} = \frac{1}{4\pi}\int \left[I(\boldsymbol{Q},\omega_\nu)^{(n)}_{\mathrm{H}}\right] d\boldsymbol{Q}, \tag{3.6}$$

where the integral is intended only on the orientation of the vector $\boldsymbol{Q}$.

Isotropic and almost isotropic oscillator approximations

The expression in eq. (3.6) is, analytically, complex, but it can be drastically simplified under particular approximations known as the *isotropic oscillator* and *almost isotropic oscillator* [149, 151]. In the first case, the mean square displacements (MSD) in the different internal modes ν_{H} are all equal to the same, value, *i.e.* $|\boldsymbol{u}_{\mathrm{H},\nu}|^2 = \bar{u}^2$ ($\forall\ \nu$). The *almost isotropic oscillator* approximation is based on the weaker assumption that $|\boldsymbol{u}_{\mathrm{H},\nu}|^2 \approx \bar{u}^2$ ($\forall\ \nu$).

Using the *isotropic oscillator* approximation eq.(3.6) can be simplified as

$$I(Q,\omega_\nu)^{(n)}_{\mathrm{H}} \propto \frac{(Q^2\bar{u}^2)^n}{n!}e^{-Q^2\bar{u}^2} \quad \forall\nu. \tag{3.7}$$

If $Q^{(n)}_{(max)}$ is the value of Q which maximizes $I(Q,\omega)^{(n)}$, by derivation of eq. (3.7) it can be shown that

$$Q^{(n)}_{\mathrm{max}} = \sqrt{n/\bar{u}^2} \quad \forall\nu \Rightarrow Q^{(n)}_{\mathrm{max}} = \sqrt{n}\ Q^{(1)}_{\mathrm{max}}. \tag{3.8}$$

As a graphical example, figure 3.2 shows the Q-profiles, *i.e.* scattering intensity as a function of Q, calculated using eq. (3.7), for $n = 1$, 2 and 3, and with $\bar{u}^2 = 1.9\cdot10^{-2}$ Å^2 .[(d)] The maximum of the curves occurs at higher Q values when the order of the transition increases, as expected from eq. (3.8).

Using the weaker assumptions of the *almost isotropic oscillator* approxi-

[(d)] The value for $\bar{u}^2$ was calculated from $u^2_{\mathrm{H},\nu} = \hbar/\left(4\pi m_{\mathrm{H}}\right)\cdot\nu_{\mathrm{H}}^{-1}$, where m_{H} is the hydrogen mass and ν_{H} was here chosen = 110 meV, *i.e.* comparable with Ti-H vibrational frequencies in $BaTiO_{3-x}H_x$.

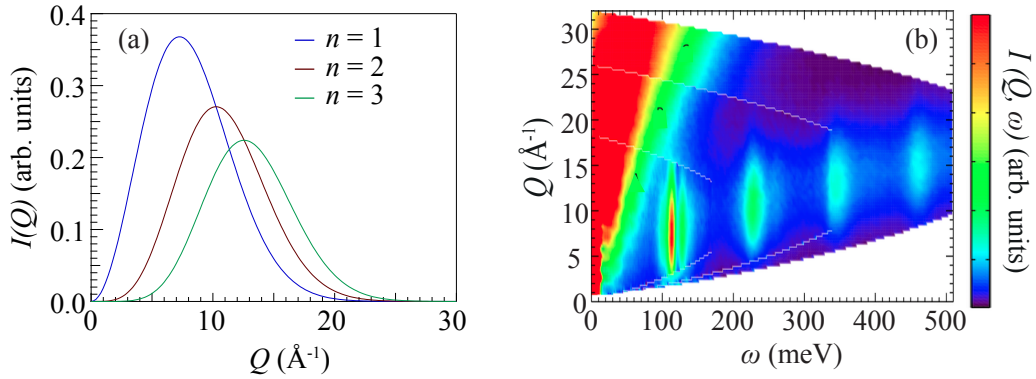

Figure 3.2: (a) Theoretical Q-profiles calculated for fundamental vibrations ($n = 1$) and their first and second overtones ($n = 2$, $n = 3$) of an isotropic oscillator. (b) INS intensity $I(Q, \omega)$ of a powder sample of $BaTiO_{3-x}H_x$ [Paper III]. The INS intensity is shown according to the color-code bar.

mation eq.(3.6) can be simplified as [149, 151]

$$I(Q,\omega)_{\mathrm{H}}^{(n)} = Q^{2n}\gamma_{\mathrm{H}}^{(n)} e^{-Q^2\alpha_{\mathrm{H}}^{(n)}}. \tag{3.9}$$

For fundamental modes ($n = 1$, $\omega = \omega_\nu$)

$$\gamma_{\mathrm{H},\nu}^{(1)} \propto u_{\mathrm{H},\nu}^2, \quad \alpha_{\mathrm{H},\nu}^{(1)} = \frac{1}{5}\left(u_{\mathrm{H,tot}}^2 + 2u_{\mathrm{H},\nu}^2\right), \tag{3.10}$$

where

$$u_{\mathrm{H,tot}}^2 = u_{\mathrm{H,int}}^2 + u_{\mathrm{H,ext}}^2, \quad u_{\mathrm{H,\ int}}^2 = \sum_n u_{\mathrm{H},\nu}^2. \tag{3.11}$$

$u_{\mathrm{H,tot}}^2$, $u_{\mathrm{H,\ int}}^2$ and $u_{\mathrm{H,ext}}^2$ are the total, internal and external MSDs, respectively.

For first order overtones ($n = 2$, $\omega = 2\omega_\nu$) and binary combination modes ($n = 2$, $\omega = \omega_\nu + \omega_{\nu'}$) the coefficients α_{H} and γ_{H} are given by

$$\gamma_{\mathrm{H},\nu}^{(2)} \propto u_{\mathrm{H},\nu}^4, \quad \alpha_{\mathrm{H},\nu}^{(2)} = \frac{1}{7}\left(u_{\mathrm{H,tot}}^2 + 4u_{\mathrm{H},\nu}^2\right), \tag{3.12a}$$

$$\gamma_{\mathrm{H,comb}}^{(2)} \propto u_{\mathrm{H},\nu}^2 u_{\mathrm{H},\nu'}^2, \quad \alpha_{\mathrm{H,comb}}^{(2)} = \frac{1}{7}\left(u_{\mathrm{H,tot}}^2 + 2u_{\mathrm{H},\nu}^2 + 2u_{\mathrm{H},\nu'}^2\right). \tag{3.12b}$$

Differentiation of Eq. (3.9) leads to

$$Q_{\max}^{(n)} = \sqrt{n/\alpha_{\mathrm{H}}^{(n)}}. \tag{3.13}$$

Note that if $u_{\mathrm{H,ext}}^2$ is negligible $u_{\mathrm{H,tot}}^2 \approx 3\bar{u}^2$ and $\alpha_{\mathrm{H},\nu}^{(1)} \approx \alpha_{\mathrm{H},\nu}^{(2)} \approx \alpha_{\mathrm{H,comb}}^{(2)} \simeq \bar{u}^2$, leading to

$$Q_{\max}^{(n)} \approx \sqrt{n/\bar{u}^2}. \tag{3.14}$$

In this thesis, equations derived within the *almost isotropic oscillator* approximation were used for the study of the hydride ion vibrational modes in $BaTiO_{3-x}H_x$, and the analysis of the Q-dependence was used to extract information about the MSD characteristic of the hydride ion. As an example, the INS intensity as function of both Q and ω measured for a sample of $BaTiO_{3-x}H_x$ is shown in Figure 3.2. The contribution at ≈ 110 meV are assigned to fundamental modes, and those at higher energies, *i.e.* ≈ 220 and 330 meV, to overtones. The maximum intensity occurs at higher Q values when the order of the transition increases, as expected.

The general case

For the majority of the cases eq. (3.6) cannot be further simplified, as in the case of O-H vibrations in acceptor doped $BaZrO_3$. However, some of the results obtained so far are extendable, at least qualitatively, to such more complex scenarios. To give an example, Q-profiles were calculated using Eq. (3.6) with $|\boldsymbol{u}_{\mathrm{H},\nu=1}| = |\boldsymbol{u}_{\mathrm{H},\nu=2}| = 0.182$ Å and $|\boldsymbol{u}_{\mathrm{H},\nu=3}| = 0.071$ Å,[(e)] and for $n = 1$ and 2. The calculated curves are shown in Figure 3.3, and the values of $Q_{\max}^{[\nu,n]}$ relative to the curves are summarized in Table 3.2. For comparison, the INS intensity as function of both Q and ω measured for a 50In/BZO sample is also shown in Figure 3.3. One can observe that the values of $Q_{\max}$ occur at a higher Q value for higher order transitions ($n \geqslant 2$), compared to the corresponding fundamental modes ($n = 1$), in agreement with the previous results. Further, $Q_{\max}$ increases when $|\boldsymbol{u}|$ decreases, in agreement with the dependence shown in eq. (3.8) and eq. (3.14).

The generality of the behavior of $Q_{\max}^{(n)}$ as a function of n and u, as illustrated above, is an important result in INS spectroscopy, showing that the study of the Q-profiles can provide a mean to distinguish between fundamental modes ($n = 1$) and higher-order transitions ($n \geqslant 2$) [149].

[(e)] The values of $|\boldsymbol{u}_{\mathrm{H},1}|$, $|\boldsymbol{u}_{\mathrm{H},2}|$ and $|\boldsymbol{u}_{\mathrm{H},3}|$ reflect the calculated root mean-square displacement of δ(O-H) and ν(O-H) modes in 50In/BZO [73].

Table 3.2: Values of $Q_{\max}$ relative to the curves shown in Figure 3.3(a)

	fundamental ($n = 1$)		overtones ($n = 2$)	
	$\nu = 1$	$\nu = 3$	$\nu = 1$	$\nu = 3$
$Q_{\max}$ [Å^{-1}]	7.3	9.5	10.2	15

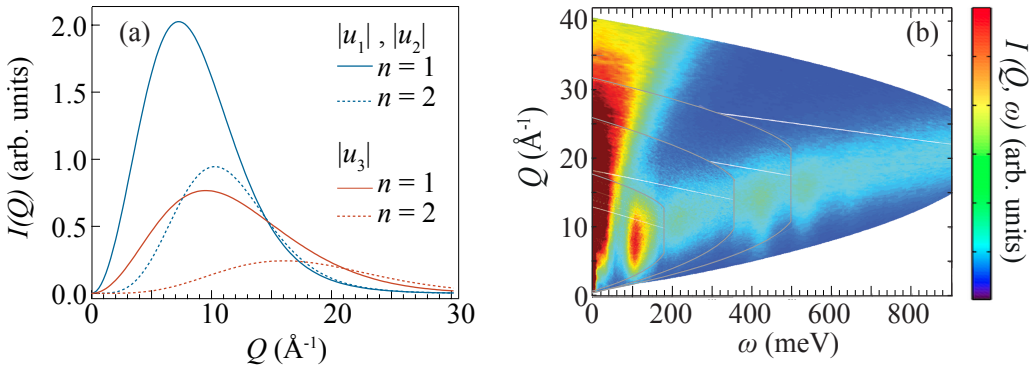

Figure 3.3: (a) Theoretical Q-profiles for fundamental harmonic O–H vibrations ($n = 1$) and their overtones ($n = 2$) in 50In/BZO [73]. (b) INS spectrum of hydrated 50In/BZO powder [Paper I].

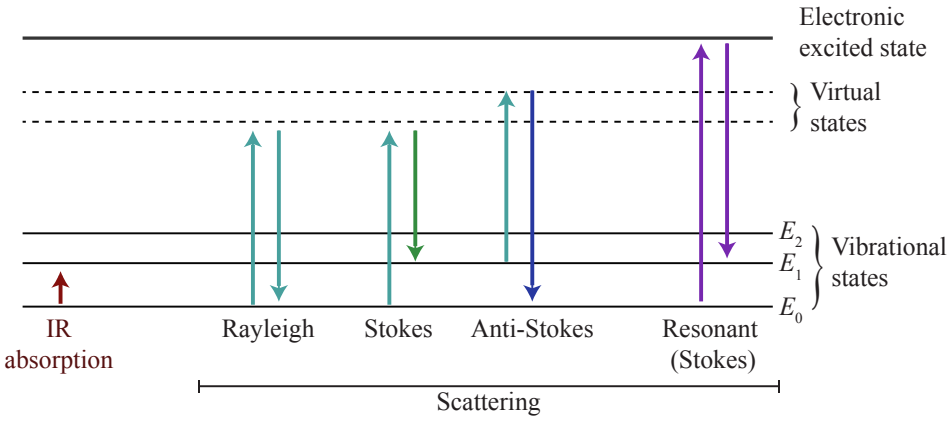

Figure 3.4: Schematic illustration of the energy transitions characteristic of IR and Raman spectroscopy, as described in the text. E_0, E_1 and E_2 label the energies corresponding to fundamental and excited vibrational states, respectively.

3.2.2 Optical spectroscopy

Infrared spectroscopy

[f]IR spectroscopy relies on the resonant interaction between IR radiation, $\lambda \in [700\text{ nm} - 1\text{ mm}]$, and matter. When the energy $h\nu_0$ of the incident light matches the energy $h\nu (= E_1 - E_0)$ of a vibrational transition, see Figure 3.4, the light-matter interaction results in the absorption of some of the incident light. By measuring how much IR light has been absorbed, scattered or transmitted from a sample at different frequencies one can gain information about the vibrational modes characteristic of the sample.

From a fundamental point of view, absorption occurs when the dipole moment, $\boldsymbol{\mu} (= \sum_i e_i \boldsymbol{r}_i)$, of a vibrating moiety oscillates at the same frequency as the electromagnetic (IR) radiation, where e_i and $\boldsymbol{r}_i$ are the atomic charges of the atom involved in the vibration and their relative atomic positions. The measured intensity of a vibrational band is proportional to the square of the change induced in the dipole moment. Vibrational modes which are not causing any change in the dipole moment are therefore normally not observable with IR spectroscopy.

[f]An exhaustive description of IR and Raman spectroscopy can be found in several textbooks, *e.g.* Refs. [152–155], which are also the main references for this section.

Raman spectroscopy

Raman spectroscopy is based on the inelastic (Raman) scattering of light from a sample. Elastic scattering, *i.e.* with no exchange of energy, is referred to as Rayleigh scattering. Raman scattering is further divided into Stokes and anti-Stokes scattering, depending on whether the material gains or loses energy. Upon inelastic scattering the energy absorbed or lost by the material corresponds to the energy $h\nu(= E_1 - E_0)$ of an excited vibrational state.

Raman scattering relies on the fact that the interaction between the electromagnetic field ϵ and a sample induces a dipole moment $\mu_{\text{ind}} = \alpha\epsilon$ in the material, where α is the polarizability of the sample. The process can be described (see Figure 3.4) as the excitation of an intermediate, virtual, vibrational state. De-excitation of this intermediate state may occur by returning to the initial state or to a state with energy higher or lower than the initial one, corresponding to the Rayleigh, Stokes and anti-Stokes scattering, respectively. Rayleigh scattering includes the majority of the scattered light, and Stokes scattering is usually more intense than anti-Stokes scattering. Further, Raman scattering only occurs for vibrations that modulate the polarizability of the sample.

A variation of "traditional" Raman spectroscopy, as described above, is resonance Raman spectroscopy. Conversely to "traditional" Raman, where the scattering of the light occurs via excitation of virtual states, in resonance Raman scattering the incident photon energy is tuned to overlap with (or be very close to) an electronic transition present in the sample, as shown in Figure 3.4, which typically means in the ultraviolet (UV) region. Under resonant conditions, the intensity of the Raman spectra can be greatly enhanced. Further, since a real electronic transition is excited, different selection rules apply, and Raman silent modes can become active in a resonance Raman spectrum.

3.3 Profiling techniques

3.3.1 X-ray and neutron reflectivity

Reflectivity techniques can be used to probe simultaneously the thickness and composition depth profile of a sample, and rely on the study of the interference pattern generated from the presence of multiple reflections in a system.[(g)]

Figure 3.5 shows a schematic example of a reflectivity experiment in the case of a system with two interfaces, of thickness h, *e.g.* a film on an "infinitely

[(g)] The following introduction to the basic principle on reflectivity is mainly after Ref. [156].

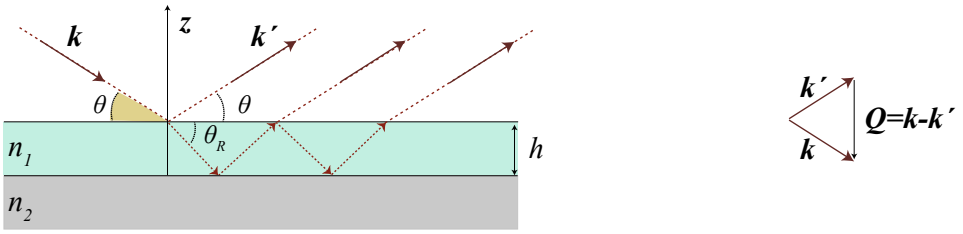

Figure 3.5: Schematic depiction of the reflectivity process from a system with two interfaces. $\boldsymbol{k}$, $\boldsymbol{k'}$ and $\boldsymbol{k}_R$ are the wavevectors of the incident, reflected and refracted waves, θ and θ_R are the angles of the incident and refracted light, and $\boldsymbol{Q} = \boldsymbol{k} - \boldsymbol{k'}$ is the transferred wavevector.

thick" substrate. The incident beam (X-ray or neutron) is characterized by its wavelength λ and wave vector $\boldsymbol{k}$, with $|\boldsymbol{k}| = 2\pi/\lambda$. The angle θ between the beam and the vacuum-sample interface is referred to as the incident angle, and n_1 and n_2 are the refractive indices of the sample and the substrate, respectively. The refractive index can be expressed as $n = 1 - \delta - i\beta$, where the terms δ and β describe the dispersive (refractive) and absorptive aspects of the light- or neutron-matter interaction, respectively. In the case of X-rays as incident radiation, $\delta_{XR} \propto eSLD$, whereas for neutron as incident radiation $\delta_N \propto nSLD$, where $eSLD$ and $nSLD$ are the electronic and neutron scattering length densities, respectively. The term β will be, for now, ignored. At the vacuum-sample interface, Figure 3.5, part of the beam is reflected at an angle θ and part is refracted at an angle θ_R, where $\cos(\theta) = n_1 \cos(\theta_R)$.

Once in the sample, the beam can be reflected multiple times at both interfaces, and part of these reflections may emerge from the sample and contribute to the total reflected intensity. As it can been seen in the example of Figure 3.5, these multiple reflections are characterized by a fixed path difference, which is a function of h and θ. In a typical specular reflectivity experiment the measured quantity is the ratio between the total reflected and incident intensities, referred to as absolute reflectivity. This is usually expressed as $R(\theta)$ or $R(Q_z)$, where $Q_z = 4\pi \sin(\theta)/\lambda$ is the modulus of the transferred wave vector.

If the quantity n_1, n_2 and h are known, it is then possible to calculate $R(Q_z)$ for the system of Figure 3.5. This requires to solve the equations describing the propagation of radiation and using proper boundary conditions at the interfaces. As an example, Figure 3.6 (a) shows $R(Q_z)$ as calculated for a 50 nm thick layer of 50In/BZO on top of an "infinitely thick" layer of MgO. The presence of a path difference between the different multiple refections produces

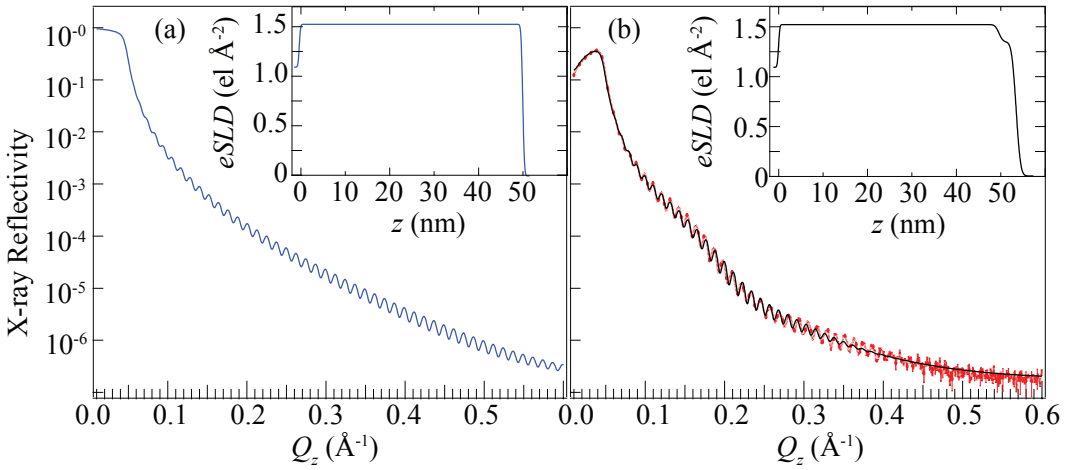

Figure 3.6: (a) XRR curve generated for a uniform, 50 nm thick layer of 50In/BZO on top on an infinitely thick MgO layer using the GenX software [157]. The corresponding $eSLD$ profile is shown in the inset. (b) XRR curve as measured on a thin film ($\approx$ 50 nm) of 47In/BZO on a MgO substrate, together with the best fit and the calculated $eSLD$ profile [Paper IV].

an interference pattern, as a function of θ, in the total reflected intensity. This results in an oscillating term in $R(Q_z)$, of periodicity $\Delta Q_z = 2\pi/h$, where the oscillations are usually referred to as Kiessig fringes. The Kiessig fringes of the reflectivity curve in Figure 3.6 (a) have a period of ≈ 0.012 Å^{-1}. Another characteristic feature of the reflectivity curve in Figure 3.6 (a), and in general of any reflectivity curve, is the presence of an initial plateau, which is related to the existence of a critical angle θ_c, and a critical Q_z value Q_c, such that $R(\theta) = 1$ for $\theta < \theta_c$. In the example of Figure 3.6 (a) Q_c is ≈ 0.05 Å^{-1}.

Similarly to the case of only two interfaces, *i.e.* a single layer, $R(Q_z)$ for a layered system depends on the values of the refractive indices (n) and the thicknesses (h) of the different layers. If, for a specific system, all these parameters are know, the corresponding reflectivity curve $R(Q_z)$ can be calculated. It follows that, in principle, from the study of $R(Q_z)$ one can obtain information about the refractive indices, and, therefore, the SLD, of each layer in a layered system.

More generally, from the analysis of a specular reflectivity curve one should be able to obtain the depth profile of the SLD, $SLD(z)$, in a sample. This depth profile can be interpreted as a composition depth profile when the scat-

tering lengths of the constituent atoms are known, *i.e.*

$$eSLD(z) = \sum_{i=1}^{m} f_i \rho_i(z), \quad nSLD(z) = \sum_{i=1}^{m} b_{\mathrm{coh},i} \rho_i(z), \tag{3.15}$$

where $\rho_i(z)$, f_i and $b_{\mathrm{coh},i}$ are the number density, the electronic scattering factor and coherent neutron scattering length of the atomic species i. However, by increasing the complexity of the structure, *e.g.* by introducing more than two layers, an uneven depth profile, roughness at the interfaces, and/or absorption in the sample, the analytical expression of $R(Q_z)$ becomes more and more challenging, and, with respect to the example above, the interpretation less straightforward. In 1954, Parrat proposed a recursive method that, starting from a reflectivity curve, yields the SLD as a function of depth in layered structures [158].

A real example of a XRR curve, as measured on a 50 nm thin film of 47In/BZO on a MgO substrate, is shown in Figure 3.6 (b). The steeper decay of the reflectivity curve and a damping of the Kiessig fringes, with respect to the example in Figure 3.6 (a), are (mainly) resulting from surface roughness. The beating in the curve reveals the presence of an inhomogeneity in the $eSLD$, which is shown in the inset of Figure 3.6 (b). The initial rise of the intensity is a well known instrumental effect due to over illumination, *i.e.* when only a portion of the beam is illuminating the sample, so that the effective incident intensity is only a fraction of the total available incident intensity.

3.3.2 Nuclear reaction analysis

[(h)]Nuclear reaction analysis (NRA) *via* the $^{1}\mathrm{H}(^{15}\mathrm{N},\alpha\gamma)^{14}\mathrm{C}$ reaction is a technique that can be used to determine the hydrogen content and depth profile inside a material. The nuclear reaction[(i)] occurs when the ^{15}N atoms are accelerated to the resonance energy $E_R = 6.385$ MeV, and produces γ-rays characterized by an energy $E_{\gamma,\mathrm{res}} \approx 4.4389$ MeV.

During a NRA experiment a beam of nitrogen nuclei, ^{15}N, is accelerated towards a sample, where the measured experimental quantity is the γ count rate, $I_\gamma(E_N)$, as a function of the energy of the nitrogen beam. For depth profiling the ^{15}N nuclei are accelerated to energies $E_N > E_R$. If the ^{15}N nuclei have energy $E_N = E_R$, they will undergo the nuclear reaction with ^{1}H close to

[(h)]Here it follows a description of the basic principles of nuclear reaction analysis, mainly after the approach of Ref. [159].

[(i)]The complete nuclear reaction is $^{1}\mathrm{H} + {}^{15}\mathrm{N} \rightarrow {}^{16}\mathrm{O} \rightarrow {}^{12}\mathrm{C} + \alpha + \gamma$.

the surface of the sample, whereas nuclei with $E_N > E_R$ will penetrate into the sample. In the sample, these nuclei will lose energy because of their interaction with matter, which is described by the material's electronic stopping power s. Once the nuclei reach the resonance energy, the reaction can occur. In a simplistic description, the energy loss (ΔE) is proportional to the trajectory length in the sample, z, and the stopping power, *i.e.* $\Delta E(z) = s \cdot z$, and the resonance occurs when $\Delta E(z) = E_N - E_R$. The γ count rate measured for a specific E_N is directly proportional to the concentration of hydrogen atoms $n_H(z)$ at the depth z where the reaction occurs, *i.e.*

$$I_\gamma(E_N) \propto \int \delta\left(E_N - E_R - z \cdot s\right) n_H(z) dz. \tag{3.16}$$

In a more realistic description the δ distribution is substituted by Lorentzian-shaped cross section of the reaction. One should also take into account that the ion beam is not perfectly monochromatic, rather the energy is distributed around the nominal energy E_N. Further, the energy distribution increases while the ^{15}N nuclei travel inside the material, due to the stochastic nature of the interaction with the electrons. Accordingly, the δ distribution is replaced by an effective instrumental function F, i.e.

$$I_\gamma(E_N) \propto \int F(E_N, z) n_H(z). \tag{3.17}$$

To obtain the absolute concentration of ^{1}H one must compare the γ count rate with measurements on a reference sample with known composition and H content. The precision of NRA measurements is influenced by the quality and the uncertainty about the calibration sample serving as a reference, but the accuracy of the method is extremely high and only limited by the statistical uncertainty related to the γ count rate.

3.3.3 Depth profiling in proton conducting oxides

In this thesis, the combination of XRR, NR and NRA has been used to determine the composition depth profile in hydrated, deuterated and dehydrated films of 47In/BZO. A key property of NR, with respect to this work, is the large neutron cross section of hydrogen and deuterium, and the large contrast between the coherent scattering length densities of these two elements (table 3.1). Conversely to the neutron cross section, the X-ray cross section is larger for heavier elements. This means that NR is highly sensible to the

hydrogen/deuterium insertion and desorption, whereas XRR gives mainly information about the composition of the perovskite host, *i.e.* the concentration depth profile of Ba, Zr and In. NR and NRA measurements can both provide an (independent) assessment of the hydrogen concentration depth profile. NR offers much higher depth resolution than NRA, whereas NRA gives a much accurate estimation of the hydrogen content depth profile.

In the work reported in this thesis, NR was used to estimate the average bulk hydrogen concentration, and this value was used to calibrate the NRA measurements.

Chapter 4

Instrumentation

4.1 INS spectrometers

In this thesis three INS spectrometers were used, MERLIN and TOSCA, both available at the ISIS Pulsed Neutron and Muon Source (STFC Rutherford Appleton Laboratory, U.K.) and VISION, available at the Spallation Neutron Source (SNS) at the Oak Ridge National Laboratory, U.S.[(a)] All three instruments are based on the time-of-flight (TOF) technique, meaning that the energy E of the neutrons is derived by measuring the time Δt they need to cover a certain, known, distance ΔL, *i.e.*

$$E = \frac{1}{2} m_N \left(\frac{\Delta L}{\Delta t} \right)^2 ,$$

where m_N is the mass of the neutron.

MERLIN is a medium resolution direct geometry spectrometer, which indicates that the energy of the incoming neutrons is fixed, and the INS intensity is measured for different final energies. Incident neutrons with (nominally) the same energy are usually obtained from an incident white beam by using a chopper or a monochromator, see Figure 4.1 (a). This type of spectrometer is suitable for simultaneous measurements of Q and $\hbar\omega$. MERLIN, specifically, is equipped with an array of detectors to cover a large angular range, from 4° to 140°, *i.e.* it offers the possibility to explore a large Q-range and, compared to other INS spectrometers, is characterized by a large incident flux [161]. The energy of the incident neutrons can be chosen in a large range, from 7 to 2000

[(a)] Exhaustive descriptions of the INS spectrometers and their characteristics can be found elsewere, *e.g.* [149, 160].

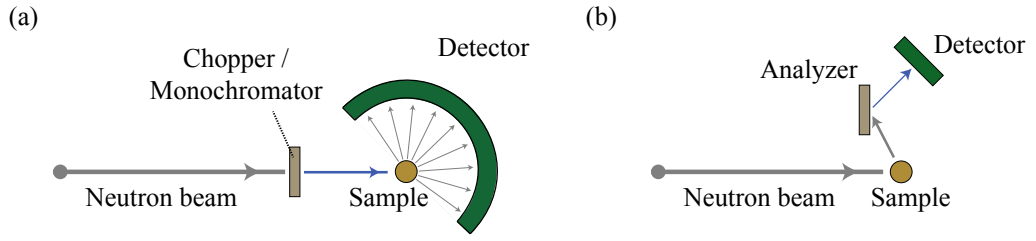

Figure 4.1: Schematic view of a direct geometry (a) and an indirect geometry (b) INS TOF spectrometer.

meV, and the instrument resolution is of the order of 3-5% of the incident energy [161].

TOSCA and VISION are high resolution indirect geometry spectrometers. These instruments use a white incident neutron beam and the scattered neutrons are detected only in a very narrow range of final energies. Neutrons with the correct, usually very low, final energy, are selected by the use of an analyzer, see Figure 4.1(b). Accordingly, they follow a specific, fixed, trajectory through (Q, ω) space. TOSCA and VISION are suitable for INS measurements with transferred energy up to approximately 1000 meV, and are characterized by a resolution of the order of 1% of the transferred energy [162–164].

In this thesis, MERLIN was used for the investigation of $I(Q, \omega)$ in the entire range of the O–H and Ti-H vibrational dynamics, including both fundamental vibrational modes and their overtones. TOSCA and VISION were employed for a more detailed investigation of the $I(\omega)$ spectra.

4.2 Optical spectroscopy

IR spectrometer

The IR measurements reported in this thesis were performed on a Bruker Alpha Fourier Transform IR (FTIR) spectrometer in diffuse reflectance configuration.[(b)] As schematically illustrated in Figure 4.2 (a), in a FTIR spectrometer a polychromatic IR light is divided into two beams, where the path difference between the beams can be varied using an interferometer. Downstream of the interferometer both beams are directed on the sample and, subsequently, on a

[(b)] An exhaustive description of this instrument can be found elsewhere [153, 154].

detector. An interference pattern is recorded as a function of the path difference, and the Fourier transformation of it yields a vibrational spectrum, *i.e.* intensity *vs* frequency [153, 154, 165]. The measurements can be performed in two modes of operation: reflectance (specular or diffuse) and transmittance, see Figure 4.2 (a). Measurements in diffuse reflectance mode, as the ones performed in this thesis, are most suitable for powder samples and are realized by blocking the specularly reflected light.

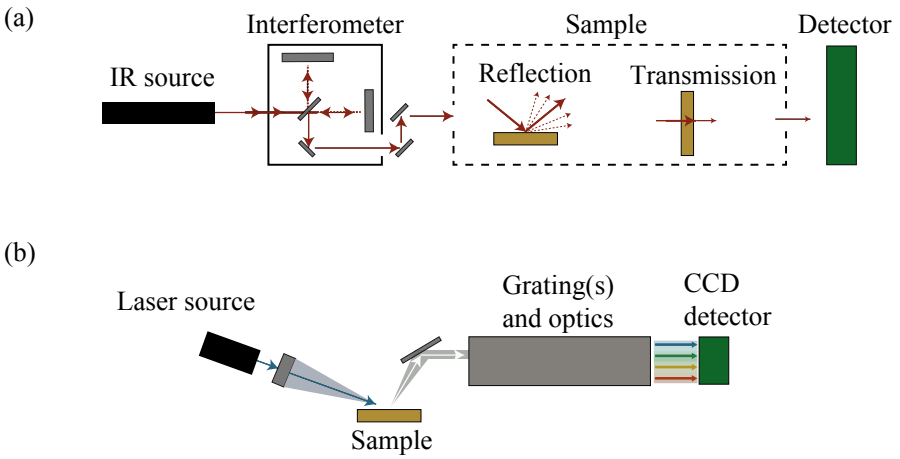

Figure 4.2: Simplified schemes of (a) a FTIR spectrometer with reflectance (specular or diffuse) and transmittance modes of operation and (b) a back-scattering geometry Raman spectrometer (b).

Raman spectrometers

The Raman spectroscopy measurements reported in this thesis were performed, at room temperature, on a triple-grating Dilor XY 800 spectrometer equipped with a tunable Ar+/Kr+ laser generating linearly polarized light. The spectra presented in this thesis were collected using light with an incident wavelength of 514 nm. During an experiment the light is focused onto the sample by a microscope, and the backscattered signal is collected in a triple grating system. A schematic depiction of a Raman spectrometer in back-scattering geometry is given in Figure 4.2 (b). The spectrometer can be used in different types of operation, distinguished by different optical paths and detected spectral

windows. The dispersed light is collected onto a CCD detector cooled by liquid nitrogen.

The resonance Raman spectroscopy experiments reported in this thesis were performed in backscattering geometry using the custom made equipments at the CFEL - Center for Free Electron Laser Science, in Hamburg. The setup uses a two laser system and an intracavity as a frequency doubling unit, and gives access to exciting energies between 1.55 eV and 6.19 eV (*ca.* 200-800 nm). A detailed description of the set-up can be found in Ref. [166].

4.3 Neutron reflectometers

Neutron reflectometers can be divided into two main groups of instruments: monochromatic instruments and TOF instruments. In the first case, neutrons with a specific wavelength (λ) are used and the reflectivity is measured at the specular condition as a function of the incident angle θ by rotating both the sample and the detector (see Figure 4.3). In TOF measurements, the incident angle θ is fixed and a polychromatic pulsed beam is used. The reflectivity data is collected as a function of the traveling time Δt, over a distance ΔL, and converted to $R(Q_z)$ through the relationship

$$Q_z = m_N \frac{\Delta L}{\Delta t} \cdot \frac{4\pi \sin(\theta)}{h}. \tag{4.1}$$

For the NR experiments in this thesis, two different instruments were used: the polarized beam reflectometer (PBR) at the NIST Center for Neutron Research (NCNR) and the D17 reflectometer at the Institut Laue-Langevin (ILL). Both instruments are featured by a horizontal scattering geometry, meaning that the sample is held vertical and the plane containing the incident and reflected beams is horizontal, as illustrated in Figure 4.3. The PBR reflectometer exploits a monochromatic beam ($\lambda = 4.786$ Å) [167, 168], whereas D17 allows measurements in either monochromatic or TOF mode [169, 170].

A key aspect of TOF instruments is that they allow to collect data over a fairly large Q-range in a relatively short time. However, the simultaneous measurements over a large Q-range usually results in reflectivity data having different statistics at low and high values of Q_z. Using a monochromatic instrument it is possible to set different measuring times for different Q_z values, thus obtaining similar (high) statistics in the majority of the Q-range. In this thesis, the D17 spectrometer in the TOF operation mode was used to perform NR experiments while heating and cooling a sample. The simultaneous

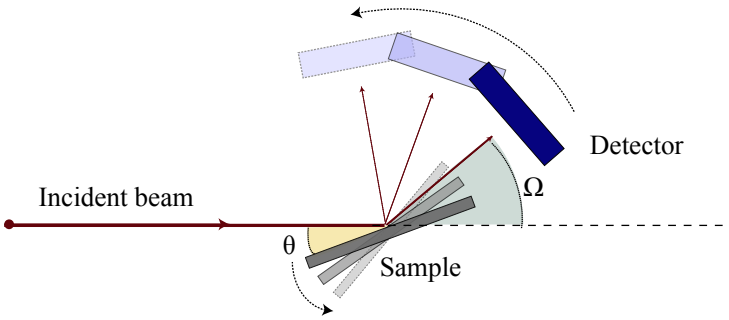

Figure 4.3: Schematic top view of a horizontal scattering geometry (vertical sample) reflectivity set-up for a monochromatic instrument, where the two independent rotational movements of the sample (θ) and of the detector (Ω) are indicated. The specular condition is obtained for $\Omega = 2\theta$.

access to a large Q-range was important for the monitoring of fast changes in the reflectivity curves, although with low statistics. This is important, for instance, in order to catch sight of fast changes in the chemical composition of the sample upon dehydration. The complementary use of the monochromatic PBR instrument provided data with higher statistics at high Q_z values ($Q_z > 0.1$ Å^{-1}), which were important to properly analyze the concentration depth profile in the samples.

Chapter 5

Results and discussion

The unifying theme of my thesis has been the study of hydrogen sites in $BaZr_{1-x}M_xO_3H_x$ and $BaTiO_{3-x}H_x$, with particular attention to the coupling between local structure and dynamics. In this chapter I discuss the main finding from this work, as well as their implications and their contribution to the current understanding of hydrogen diffusion in materials of relevance for energy application.

5.1 Local structure and dynamics in acceptor doped $BaZrO_3$

5.1.1 Vibrational spectroscopy and computer simulations

The first part of this thesis was dedicated to the investigation of proton sites in $BaZr_{1-x}M_xO_3H_x$, with M = In and Sc and $x = 0.1$ and 0.5. The work pays particular attention to the local environment and dynamics of the protons and the role of the type (M) and level (x) of doping, and was performed using INS and IR spectroscopy. Complementary AIMD simulations were performed for structural model with M = In and Sc and $x = 0.125$ and 0.5. Vibrational density of states (VDOS), which can be compared to the INS spectra, were calculated from the simulations. A key finding is that 10Sc/BZO, 10In/BZO and 50Sc/BZO are characterized by very similar O-H vibrational spectra, as exemplified in Figure 5.1. For 50In/BZO the INS spectrum shows a pronounced broadening of both O-H vibrational bands, and the IR spectrum in the ν(O-H) region exhibits two bands at 250 and 290 meV, which are absent for the other

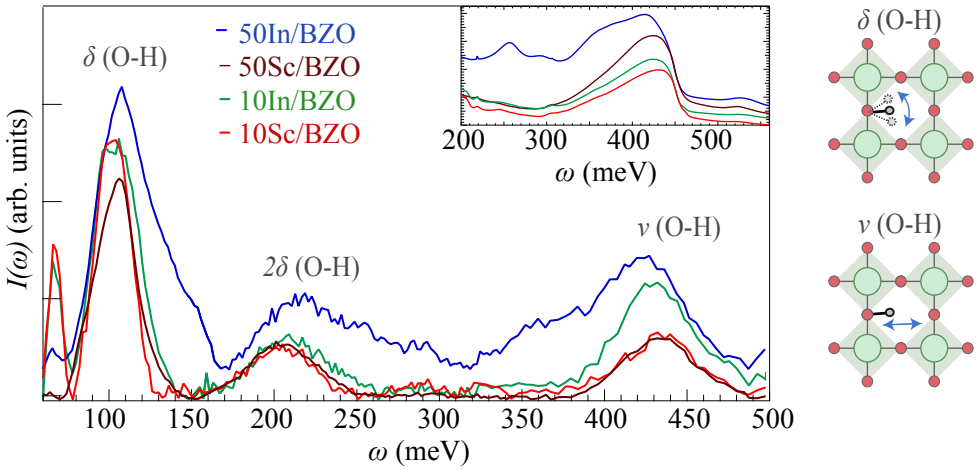

Figure 5.1: INS spectra of $BaZr_{1-x}M_xO_3H_x$ (M = In and Sc, $x = 0.1$ and 0.5), together with the band assignment and a sketch of the δ(O-H) and ν(O-H) vibrations. The spectrum of 50In/BZO is vertically offset for easier comparison. The inset shows the IR spectra of the same samples in the ν(O-H) region.

samples.

A peak-fit analysis of the INS bands, together with a detailed analysis of their Q-dependence, was used to identify spectral contributions associated to different proton sites, as shown in the example of Figure 5.2. Interestingly, the computational results revealed that the hydrogen bond length ($d_{O\cdot\cdot H}$) experienced by each specific proton, together with the characteristic vibrational frequencies, vary significantly over time. In order to compare calculated and experimental vibrational frequencies, we have therefore computed the VDOS for specific ranges of $d_{O\cdot\cdot H}$, see Figure 5.3(a). Specific δ(O-H) and ν(O-H) vibrational energies were, in this way, associated to different hydrogen bond strengths. The computational results also suggest that hydrogen bond length fluctuations are mainly driven by lattice dynamics, as illustrated in the examples of Figure 5.3 (b-c). It is proposed that oxygen dynamics are most likely responsible for the fluctuations of the potential energy barrier associated to specific diffusion events, *e.g.* oxygen movements shortening (strengthening) the hydrogen bonds may favor proton hopping.

The combination of experimental and computational results revealed that in all materials the majority of protons are located in sites with weak and medium hydrogen bonding. In 50In/BZO a portion of protons is located in

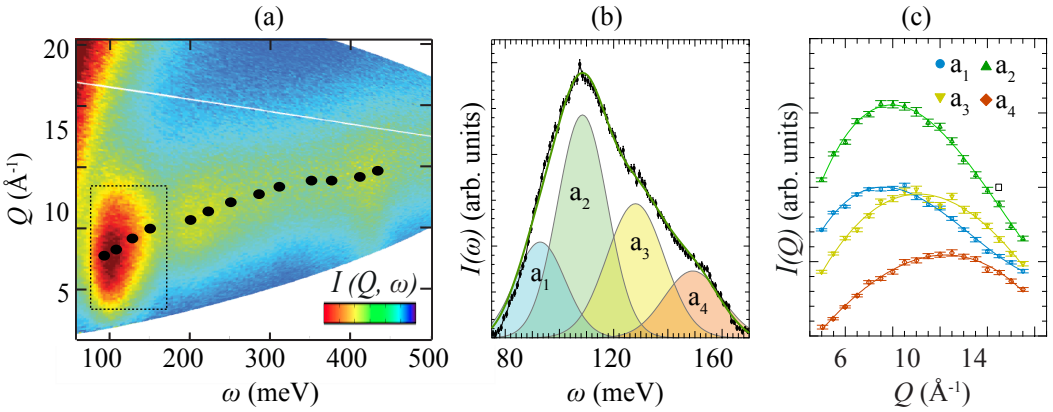

Figure 5.2: (a) INS intensity $I(Q, \omega)$ as measured for 50In/BZO together with (b) the INS spectrum and the fit to the data in the δ(O-H) energy region and (c) the corresponding Q-dependence analysis (c). a_1-a_4 are the identified peak-fitted components. The black bullets in (a) represent the values of Q which maximize the INS intensity of the bands, obtained from Q-dependence analysis. The highlighted area corresponds to the δ(O-H) modes.

additional sites with strong and very strong hydrogen bonding. These sites are compatible with the broadening effect observed in the INS spectra. We suggest that the presence of the IR peaks at 250 and 290 meV is due to the existence of a relatively small amount of protons located in structural arrangements characterized by very strong hydrogen bonding, specifically with $d_{\text{O}\cdot\cdot\text{H}} \approx 1.5$ Å. Accordingly, these peaks were assigned, for the first time, to low energy fundamental ν(O-H) vibrations. Crucially, there are few to no sites with $d_{\text{O}\cdot\cdot\text{H}} \approx 1.5$ Å within the structural arrangements considered in the simulations. This suggests that such proton sites are stabilized in some sort of "extreme", heavily distorted environments, not included in the simulations.

Interestingly, the additional proton sites observed in 50In/BZO resemble a type which can be found in hydrated $Ba_2In_2O_5$, *i.e.* $BaInO_3H$. $Ba_2In_2O_5$ exhibits a brownmillerite structure, an oxygen-deficient variant of the perovskite structure [105, 171–173], which is also adopted by In-doped BZO when the In-doping is higher than ≈75%. [73, 75, 96]. As schematically shown in Figure 5.4, in $BaInO_3H$ the proton can occupy two distinct proton sites, H(1) and H(2), where the H(1) sites are relatively similar to those found in perovskite structures. The H(2) proton site is, instead, characterized by a more distorted

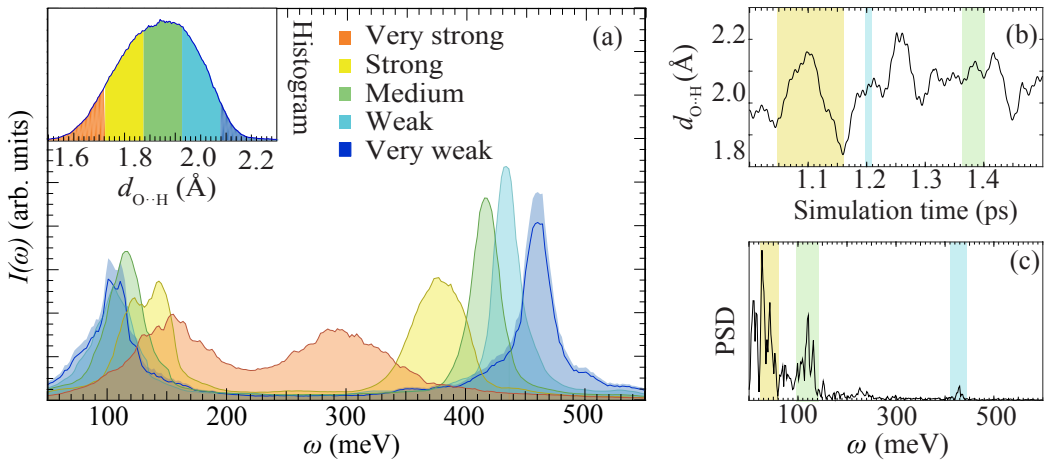

Figure 5.3: (a) VDOS obtained for specific strengths (lengths) of the hydrogen bond, as indicated in the legend. The $d_{O\cdots H}$ distribution over the simulations is shown in the inset. (b) Fluctuations of the hydrogen bond length ($d_{O\cdots H}$), as extracted from the *AIMD* simulations, and (b) corresponding characteristic frequencies, obtained by PSD analysis. The correspondence between the period of the oscillations and the characteristic frequency is highlighted in the figure.

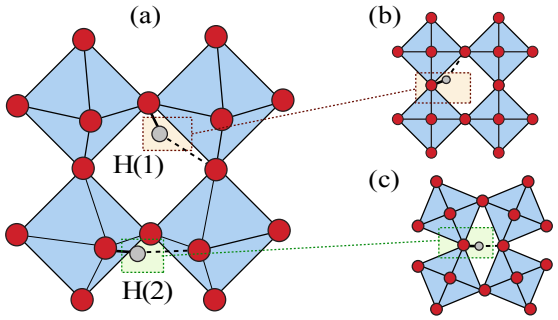

Figure 5.4: (a) Schematic drawing of the $BaInO_3H$ structure with the H(1) and H(2) proton sites, also shown in (b) and (c), respectively.

local environment and a stronger hydrogen bonding [105, 171–173]. Further, the associated ν(O-H) band is located at relatively low energies [174], and is, crucially, comparable with the extra features observed in the vibrational spectra of 50In/BZO. Since EXAFS and Raman studies suggest that there is no long-range browmillerite ordering in 50In/BZO [75, 96], it is proposed that 50In/BZO contains a small fraction of proton sites reminiscent of the H(2) site in $BaInO_3H$, but without the formation of browmillerite domains.

In contrast to In-doped BZO, Sc-doped BZO exhibits an average-cubic perovskite structure even for a complete substitution of Sc for Zr, corresponding to the $Ba_2Sc_2O_5$ material [175], and the IR spectra of 10Sc/BZO, 50Sc/BZO and 100Sc/BZO [175] are essentially the same, with no indication of H(2) sites. A recent IR investigation [78] shows that the ν(O-H) spectra of Y-doped BZO exhibit, similarly to those of Sc-doped BZO, little to no contribution in the region associated to very strong hydrogen bonding, and the increase of Y-doping level results only in a minor spectral evolution. It is suggested that for In dopants the increase of doping level leads to localized distortions and, consequently, to the population of additional proton sites, whereas for other dopants, such as Sc, the increase of doping level has much smaller impact on the proton site distribution.

We also looked at proton-proton association, and our results suggest that when protons are in close proximity to each other they may cooperatively increase the structural distortions and stabilize strong hydrogen bonds. This is in agreement with computational works on Y-doped $BaZrO_3$ [90] and $SrTiO_3$ [116], which have suggested that the protons affect each others indirectly, *via* local lattice distortion. The indirect-interaction scenario is also supported by

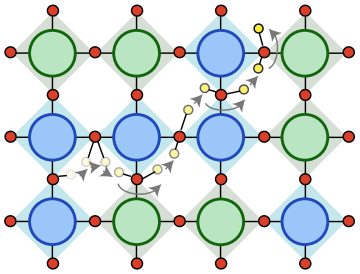

Figure 5.5: Schematic 2-D illustration of a conduction pathway for protons in the presence of a network of dopant atoms, here indicated with blue coloring. The arrows indicate the direction of the motion of the proton through the lattice

computational results on Sc-doped BZO [71]. Our work further suggests that the local distortions are dynamical, driven by both lattice and O-H vibrational dynamics.

Finally, in In50/BZO it was found that structures with protons close to dopant atoms are, generally, energetically favorable, in complete agreements with the concept of proton-trapping [34–37, 68, 71, 84–87]. However, due to the high doping level, the In atoms are percolated by design in the structural models. As also suggested by very recent computational results on Y-doped BZO [91], the presence of a network of dopant atoms creates a sort of preferential conduction pathway, as schematically illustrated in Figure 5.5, so that the diffusion of the protons away from a dopant atoms is not required even in long-range diffusion. Accordingly, the concept of proton trapping is not directly transferable to the highly doped BZO, as studied here, and the proton trapping effect is not as critical as in the low-doping limit.

5.1.2 Depth concentration profiling of thin fims

In order to obtain more insight about proton local coordination in acceptor doped BZO, I, together with my colleagues, further investigated the distribution of protons, upon hydration, in these materials. The study was performed on 50 nm thick films of 47In/BZO, grown by pulsed laser deposition, by means of NR, XRR and NRA techniques. Additionally, XRD, RBS and IS measurements, were used to investigate the structure, chemical composition and proton conductivity of the samples.

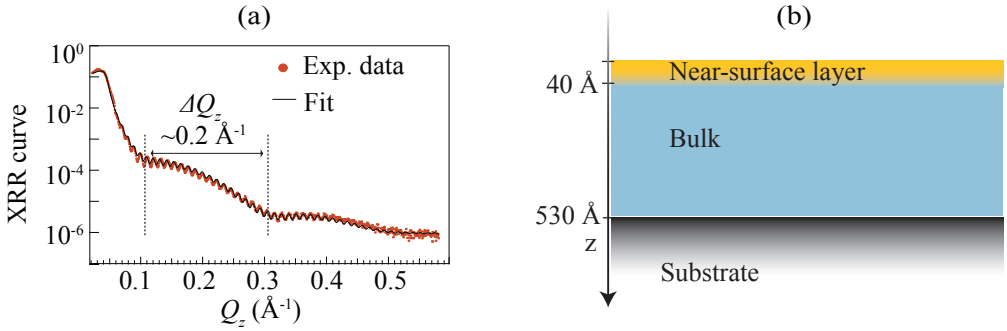

Figure 5.6: (a) XRR curve as measured on a nominally dehydrated film of 47In/BZO. The beating, of $\Delta Q_z \approx 0.2$ Å^{-1}, corresponds to a layer of thickness $d = 2\pi/\Delta Q_z \approx 30$ Å. (b) Schematic illustration of the model used to analyze the reflectivity data, with a thin near-surface layer on the top of the bulk part of the sample.

The results from XRR reveal the presence, in the film, of a sub-layer with a characteristic thickness of 30–40 Å. This is manifested in the X-ray reflectivity curves as a beating of a period of ≈ 0.2 Å^{-1}, as can be observed in the example in Figure 5.6 (a) A systematic analysis of the XRR and NR curves, based on model systems containing one, two or three layers, showed that the best model to describe the data contains a thin layer close to the surface of the sample, and a thicker layer beneath, as illustrated in Figure 5.6 (b). A model containing a single layer was not adequate to fit the data, whereas models based on more than two layers did not improve the quality of the fits. The $eSLD$ and $nSLD$, as shown in Figure 5.7 (a-b), were obtained from the best fit to the data.

These results indicate that the 3–4 nm thick layer, close to the surface of the film, is characterized by a somehow altered cationic composition. The values of the $nSLD$ for the bulk of the film are compatible with the insertion of H/D in the perovskite structure, and suggest that the bulk of the samples are fully hydrated/deuterated upon hydration/deuteration. The combination of the results from NR and NRA was used to asses the proton concentration profile in the samples upon hydration and de-hydration, which showed the presence of high-proton density in the near-surface layer. The hydrogen concentration profile, as extracted from NRA measurements, is shown in Figure 5.7 (c). According to these experimental results, the bulk of the sample absorbs and desorbs protons as anticipated, whereas the surface layer either retains or re-obtains protons after desorption.

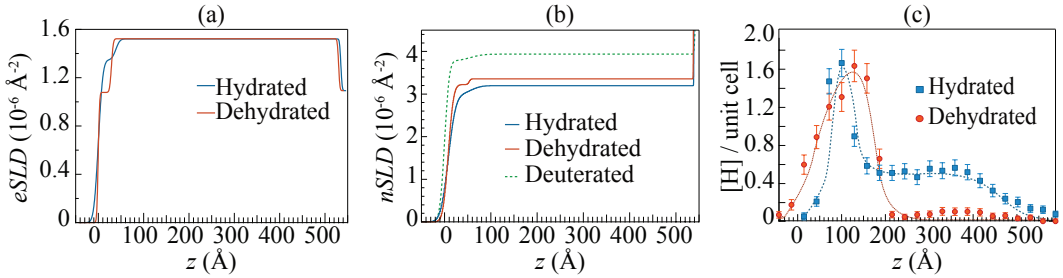

Figure 5.7: The eSLD (a) and nSLD (b) profiles as obtained from the analysis of the XRR and NR curves measured on the hydrated, dehydrated and deuterated 50 nm films of 47In/BZO. (c) Hydrogen concentration profile, expressed as hydrogen atoms per unit cell, as obtained from NRA measurements on the same samples.

The presence of residual protons also after dehydration is consistent with results from previous IR absorbance spectroscopy in the O-H stretch region [93, 95,104], and nuclear magnetic resonance [72] for the same or similar perovskite materials. Of particular relevance is that In-doped BZO shows a preferential desorption of protons experiencing strong or very strong hydrogen bonding, and that these protons are essentially gone for temperatures above *ca.* 350 °C [104]. The residual protons in the surface region of the films are therefore likely to be characterized by weak or very weak hydrogen bonding interactions.

Although the results reported here specifically concern thin films, it is not unlikely that residual protons in powder samples accumulate close to the surface of the grain. Interestingly, QENS studies of micro- and nano-crystalline samples of In-doped BZO have suggested that in the nano-crystalline samples the protons somehow accumulate on the surface and/or grain-boundary regions [127,176]. Additionally, the authors have found clear evidence of proton motion only in the microcrystalline samples, indicating that protons in the surface regions are most probably less mobile [127, 176]. The results, as discussed so far, would indicate a correlation between weak hydrogen-bonding interactions and low proton mobility, as found for the near-surface protons.

5.1.3 Resonant Raman spectroscopy

Our study on proton sites in acceptor doped BZO have suggested, in agreement with the current view in the field [7, 8, 10, 38–42, 177–179], that the lattice

dynamics are responsible for the fluctuations of the hydrogen bonds strength and, consequently, the potential barrier for proton transfer. In this context, I have also investigated the resonance and non-resonance Raman spectra of BZO and 20Y/BZO. The study was aimed to compare the Raman spectra measured for different incident photon energies, identify potential resonant energies, and to asses the potential of resonance Raman spectroscopy for the study proton conducting oxides and similar materials, with particular attention towards time resolved experiments.

For this purpose, resonance Raman experiments were performed on a 500 nm thick film of 20Y/BZO and a polycrystalline sample of BZO by using photon energies between 3.44 and 5.17 eV. Complementary measurements were performed on the BZO polycrystalline sample using visible light (2.41 eV), whereas no reliable spectrum cold be measured, in the same conditions, for 20Y/BZO. The latter was due to the fact that, since the penetration depth of the used light is of the order of 500 nm, the Raman scattering signal from the film is overwhelmed by the Raman scattering signal from the substrate.

The resonance behavior was investigated by analyzing the experimental spectra and by following the evolution of the different spectral components as a function of the photon energy, as shown in Figure 5.8. The activation of a strong resonance Raman effect is observed, in both materials, for an incident photon energy of approximately 5 eV, in agreement with the reported band gap for BZO [37, 117, 180–184]. The resonance involves all spectral components, and under resonant conditions the spectral intensity was found to be enhanced by two to three orders of magnitude. Concerning the spectral components, their number and positions did not show any apparent dependence on the incident photon energy, rather the spectral features were found to be very similar from one spectrum to another. Further comparisons with the spectra recorded using visible light (2.41 eV) have confirmed that the spectral features observed far from resonant conditions are the same as observed close to and under resonance.

Importantly, the results confirm that resonant Raman spectroscopy can be used on films, which are not always suitable for non-resonant investigation, as in the case of the 500 nm thick film of 20Y/BZO. With a view toward the future the use of resonant Raman could therefore have some critical advantages in, for instance, time-resolved experiments. First, these experiments may require the use of film samples, hence it is important to be able to rely on techniques which are suitable for these kind of samples. Additionally, by measuring close to resonant conditions one can achieve higher spectral intensity, which means reduced measuring time and lower signal-to-noise ratio, both

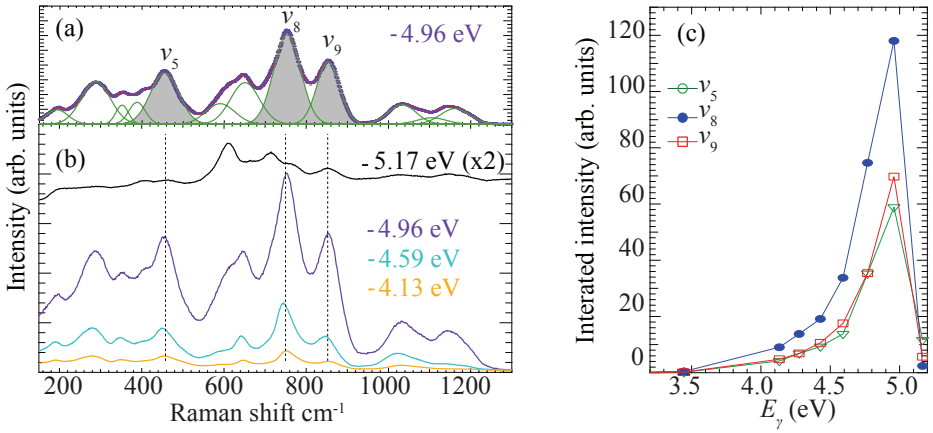

Figure 5.8: (a-b) Example of resonance Raman spectra as measured on BZO sample using different incident photon energies, together with a peak-fit analysis of the spectrum measured an 4.96 eV incident photon energy. (c) Example of evolution of the integrated intensity as a function of the incident photon energy, as obtained for the three spectral components labelled as ν_5, ν_8 and ν_9.

affecting significantly the quality of the data.

5.1.4 Final remarks

The sum of the results obtained on $BaZrO_3$-based proton conducting oxides shines new light on the local structure and dynamic processes in these materials. The defect chemistry, *e.g.* the presence of dopant atoms or protons, but also cation deficiency, is important in the formation of a variety of different local coordination environments for the protons, characterized by different length (strength) of the hydrogen bond and O-H vibrational energies. The strength of the hydrogen bond, in particular, seems to be related to the ability of the proton to (locally) diffuse, specifically weak hydrogen bonding interaction may correspond to proton with low mobility. However, the fundamental properties defining a proton sites, *e.g.* the lenght of the hydrogen bonding, are strongly affected by the fluctuation of the lattice. This implies that the lattice dynamics are of fundamental importance for the determination of the proton mobility, and, accordingly, for the proton transport properties of $BaZrO_3$-based oxides

5.2 Local structure and dynamics in $BaTiO_{3-x}H_y$

Building further on the investigation of local structure and dynamics in proton conducting perovskites, I also investigated the nature of local structure and dynamics in the perovskite oxyhydride $BaTiO_{3-x}H_y$. The specific aim was to understand the influence of hydrogen content (y) and oxygen vacancy content ($x - y$) on the local structure and dynamics of the hydride ions. For this purpose, INS vibrational spectra were recorded for four different compositions of $BaTiO_{3-x}H_y$, characterized by the simultaneous presence of hydride ions and oxygen vacancies.

The vibrational spectra were fully characterized and divided into fundamental Ti-H modes (85–160 meV), and second- and third-order transitions modes, at 180–300 meV and 300–410 meV, respectively, as shown in Figure 5.9 (a). Here, a careful analysis of both the spectral intensity $I(\omega)$ and its Q-dependence $I(Q)$ [Figure 5.9 (b)] was used to clearly distinguish between fundamental and higher-order transitionsw. The Ti-H fundamental vibrational frequencies were found at, approximately, $\omega_{\perp} = 114$ meV and $\omega_{\parallel} = 128$ meV. The assignment is supported by the comparison with vibrational frequencies obtained through DFT calculations, and is in accordance with previously published theoretical calculations [137]. Additionally, it was also shown that all hydrogen species are present as hydride ions located on vacant oxygen sites of the perovskite structure, with no indications of O-H groups or other interstitial hydrogen species present.

The INS measurements further reveal the presence of several fundamental contributions to the vibrational spectra (Figure 5.10), which is interpreted as the simultaneous presence of different local environments of the hydride ions. In order to obtain more details about these local environments, we have performed DFT calculation for structural models with and without oxygen vacancies. The vibrational energies of the hydride ions as calculated for different structural models are summarized in Figure 5.10, together with an example of two models, containing an hydride ion and a oxygen vacancy as a first nearest neighbor (1NN) and second nearest neighbor (2NN), respectively.

The combination of experimental and computational results suggests that a small portion of hydride ions is, indeed, located at sites corresponding to the 1NN and 2NN configurations. The presence of sites in the proximity oxygen vacancies is of particular relevance because it supports the claim that hydride ions can diffuse by jumping to 1NN sites, at low temperature (225 K), and to 2NN at higher temperature (500 K) [145].

Interestingly, the experimental results indicate that the site distribution is

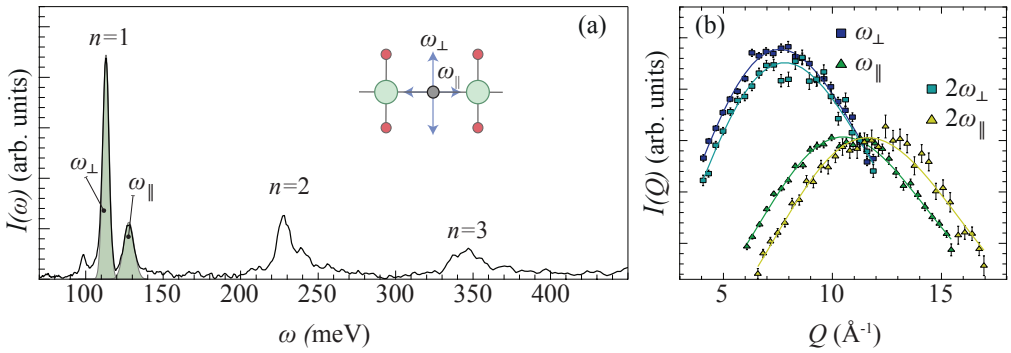

Figure 5.9: (a) INS spectra of one of the $BaTiO_{3-x}H_y$ samples, together with the assignments of the different INS bands and a sketch of the Ti-H $\omega_\perp$ and $\omega_\parallel$ vibrations. (b) Q-dependence $I(Q)$ as obtained from the INS measurements .

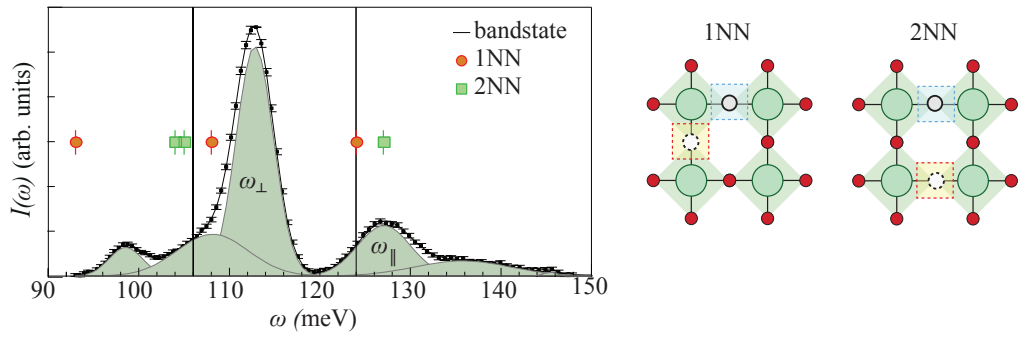

Figure 5.10: INS spectrum of one of the $BaTiO_{3-x}H_y$ samples, together with the fit of the spectrum. The presence of several spectral components is due to the presence of distinct hydride ion sites. The frequencies calculated for an hydride ion far from any oxygen vacancies, in the band state configuration, and for hydride ions with an oxygen vacancy as 1NN and 2NN are indicated in the graph. A 2D sketch of the two configurations containing oxygen vacancies is also given.

almost independent on the vacancy and hydride ion concentration. A detailed analysis of the Q-dependence for the main contributions to the INS spectra was used to extract the vibrational MSD of the hydride ions in two different samples and as a function of temperature. The values were compared with those extracted from DFT calculation, showing and excellent agreement. No apparent temperature dependence was observed for both the vibrational energies and MSDs.

In summary, the combination of the results summarized in this thesis and recently published work [51,53,137,144,145] provides a novel view about hydrogen species in perovskite oxides. In $BaTiO_3$ the formation of hydride species, located on oxygen sites, significantly perturbs the perovskite structure, which is exemplified in the fact that $BaTiO_{3-x}H_x$ does no longer change its structure over temperature, as $BaTiO_3$, but rather shows a stable cubic structure. In perovskite oxyhydrides the dynamic properties of the hydride ions are strongly affected by the presence of oxygen vacancies. Specifically, long-range diffusion at low temperature relies on the formation of structural environments with hydride ions in the proximity of oxygen vacancies.

Chapter 6

Conclusions and Outlook

To conclude, this thesis has provided new insight about the nature of hydrogen sites, and the coupling between local structure and dynamic properties, in both proton and hydride-ion conducting perovskite-type oxides. Concerning acceptor doped $BaZrO_3$, it is found that the increase of In-doping level strongly affects the proton site distribution and leads to increasing local distortions, whereas for other dopants, *e.g.* Sc and Y, the doping level has little or no impact on it. It is also argued that extended, dynamic, lattice distortions influence the properties of the proton sites and mediate proton-proton interaction. Additionally, it is found that thin films are characterized, near to the surface, by a 3-4 nm thick proton-rich layer. It is proposed that these near-surface protons are characterized by generally low mobility and weak hydrogen bonding, suggesting an important correlation between the strength of hydrogen-bonding interactions and proton mobility. The complementary study of the oxyhydride $BaTiO_{3-x}H_x$ confirms the insertion of hydride ions on oxygen sites of the $BaTiO_3$ lattice. The work also provide evidences of the presence of local configurations with oxygen vacancies as the nearest neighbors to the hydride ions, in agreement with the observed nearest or second nearest neighboring jumps of long-range hydride ion diffusion.

The combination of the results obtained for both family of perovskite-type oxides point towards some very important differences in the proton and hydride-ion transport properties. It is proposed that for the determination of the proton transport properties a key role is played by the vibrational properties of the materials, whereas the diffusion of hydride-ions crucially depends on the defect chemistry of the oxide, specifically on the presence of oxygen vacancies in the structure. Accordingly, for the design of novel proton conducting oxides it is imperative to elucidate the role of lattice and O-H vibrations in

the proton diffusion For the development of hydride-ion conducting materials, instead, it may be beneficial to elucidate which are the amounts of oxygen vacancies and hydride-ions maximizing the hydride-ion diffusions.

Besides the importance of the specific findings, a key aspect of the studies discussed above is the novelty of the proposed approach, such as the combined study of the energy and momentum dependence of the INS signal for the investigation of hydrogen sites in both proton and hydride ion conducting materials. Similarly, the combination of XRR, NR and NRA was used, for the first time, to investigate structural properties and proton sites distribution in proton conducting oxides. Finally, this work has established the presence of clear advantages in the use of resonant Raman technique, with respect to standard Raman spectroscopy, such as the higher intensity near the resonance or the fact that the technique is generally more suitable for the investigation of thin samples.

With a view towards the future, the new insight obtained into the local coordination environment and dynamics of protons in acceptor doped $BaZrO_3$ opens up to new exciting possibilities for research, such as the investigation of the coupling between O-H vibrations and proton diffusion. Specifically, following the approach described by Sphar *et al.* [7, 8] and discussed in Chapter 2, one could investigate thin film samples by means of the transient bleaching technique measurements combined with IR spectroscopy measurements, and selectively probe vibrational modes assigned to specific proton sites. Complementary, the promising results from the resonance Raman investigations have opened up to the possibility of using this technique in time-resolved experiments. For instance, IR pump - (resonance) Raman probe experiments could be used to unravel the correlation between lattice dynamics, proton vibrational dynamics and, ultimately, proton transport properties.

Further, the results obtained from the depth profiling in thin films have left unclarified the origin of the proton enriched surface region and its absorption and desorption mechanism. NR and NRA measurements during *in situ* hydration and dehydration could provide more insight in this direction. In particular, it would be of interest to perform the hydration / dehydration in several steps, allowing to study intermediate levels of hydration as well.

Acknowledgments

I would like to start by thanking my supervisor Maths for his support and for giving me the possibility to do my PhD at Chalmers. I want also to thank my colleagues and friends Carin, Daria, Yuan-Chih and Adrien. Thanks to Lars, for the inspiring discussions. I would like to thank all the people that I have worked with and that have helped me during the years. Thank to all my collaborators, Göran and Erik, Daniele, Max, Alessandro, Lorenzo, Jakob and all the group of Michael Rübhausen for your help, support and the interesting discussions. I would further like to thank the local contacts at ISIS, NIST and ILL, Stewart, Joe, Philipp, for their invaluable help. Thank you the entire KMF and OOMK group, for the interesting discussions and the friendly atmosphere. I would like to express separately my gratitude to Ezio, for his help and kindness and all the useful advices. My greatest gratitude goes to my family, for they unconditional support and affection.

Bibliography

[1] S. Woutersen, B. Ensing, M. Hilbers, Z. Zhao, and C. A. Angell, "A liquid-liquid transition in supercooled aqueous solution related to the HDA-LDA transition," *Science*, vol. 359, pp. 1127–1131, mar 2018.

[2] Q. Luo, Y.-X. Lin, P.-P. Yang, Y. Wang, G.-B. Qi, Z.-Y. Qiao, B.-N. Li, K. Zhang, J.-P. Zhang, L. Wang, and H. Wang, "A self-destructive nanosweeper that captures and clears amyloid β-peptides," *Nat. Commun.*, vol. 9, p. 1802, dec 2018.

[3] Q. Sun, B. Aguila, J. Perman, A. S. Ivanov, V. S. Bryantsev, L. D. Earl, C. W. Abney, L. Wojtas, and S. Ma, "Bio-inspired nano-traps for uranium extraction from seawater and recovery from nuclear waste," *Nat. Commun.*, vol. 9, p. 1644, dec 2018.

[4] Y. Xu, J. McSally, I. Andricioaei, and H. M. Al-Hashimi, "Modulation of Hoogsteen dynamics on DNA recognition," *Nat. Commun.*, vol. 9, p. 1473, dec 2018.

[5] A. B. Wöhri, G. Katona, L. C. Johansson, E. Fritz, E. Malmerberg, M. Andersson, J. Vincent, M. Eklund, M. Cammarata, M. Wulff, J. Davidsson, G. Groenhof, and R. Neutze, "Light-induced structural changes in a photosynthetic reaction center caught by Laue diffraction.," *Science*, vol. 328, pp. 630–3, apr 2010.

[6] S.-C. Li, L.-N. Chu, X.-Q. Gong, and U. Diebold, "Hydrogen bonding controls the dynamics of catechol adsorbed on a TiO_2(110) surface.," *Science*, vol. 328, pp. 882–4, may 2010.

[7] E. J. Spahr, L. Wen, M. Stavola, L. Boatner, L. C. Feldman, N. H. Tolk, and G. Lüpke, "Giant Enhancement of Hydrogen Transport in Rutile TiO_2 at Low Temperatures," *Phys. Rev. Lett.*, vol. 104, p. 205901, may 2010.

[8] E. J. Spahr, L. Wen, M. Stavola, L. Boatner, L. C. Feldman, N. H. Tolk, and G. Lüpke, "Proton Tunneling: A Decay Channel of the O-H Stretch Mode in $KTaO_3$," *Phys. Rev. Lett.*, vol. 102, p. 075506, feb 2009.

[9] L. Malavasi, C. A. J. Fisher, and M. S. Islam, "Oxide-ion and proton conducting electrolyte materials for clean energy applications: structural and mechanistic features.," *Chem. Soc. Rev.*, vol. 39, pp. 4370–87, nov 2010.

[10] T. Norby, M. Wideroe, R. Glockner, and Y. Larring, "Hydrogen in oxides.," *Dalton Trans.*, pp. 3012–8, oct 2004.

[11] P. T. N. Kochetova, I. Animitsa, D. Medvedev, A. Demin, "Recent activity in the development of proton-conducting oxides for high-temperature applications," *RSC Adv.*, vol. 6, no. 77, pp. 73222–73268, 2016.

[12] B. C. Steele and A. Heinzel, "Materials for fuel-cell technologies.," *Nature*, vol. 414, pp. 345–52, nov 2001.

[13] T. Norby, "Solid-state protonic conductors: principles, properties, progress and prospects," *Solid State Ionics*, vol. 125, pp. 1–11, oct 1999.

[14] K. Kreuer, "Proton Conductivity: Materials and Applications," *Chem. Mater.*, vol. 8, pp. 610–641, jan 1996.

[15] J. L. Liu, S. Bashir, and J. Liu, *Advanced Nanomaterials and their Applications in Renewable Energy*. Elsevier, 2015.

[16] C. Duan, J. Tong, M. Shang, S. Nikodemski, M. Sanders, S. Ricote, A. Almansoori, and R. O'Hayre, "Readily processed protonic ceramic fuel cells with high performance at low temperatures.," *Science*, vol. 349, pp. 1321–6, sep 2015.

[17] A. Volkov, E. Gorbova, A. Vylkov, D. Medvedev, A. Demin, and P. Tsiakaras, "Design and applications of potentiometric sensors based on proton-conducting ceramic materials. A brief review," *Sensors Actuators B Chem.*, vol. 244, pp. 1004–1015, 2017.

[18] Z. Tao, L. Yan, J. Qiao, B. Wang, L. Zhang, and J. Zhang, "A review of advanced proton-conducting materials for hydrogen separation," *Prog. Mater. Sci.*, vol. 74, pp. 1–50, 2015.

[19] H. Malerød-Fjeld, D. Clark, I. Yuste-Tirados, R. Zanón, D. Catalán-Martinez, D. Beeaff, S. H. Morejudo, P. K. Vestre, T. Norby, R. Haugsrud, J. M. Serra, and C. Kjølseth, "Thermo-electrochemical production of compressed hydrogen from methane with near-zero energy loss," *Nat. Energy*, vol. 2, pp. 923–931, dec 2017.

[20] L. Bi, S. Boulfrad, and E. Traversa, "Steam electrolysis by solid oxide electrolysis cells (SOECs) with proton-conducting oxides," *Chem. Soc. Rev.*, vol. 43, pp. 8255–8270, aug 2014.

[21] S. H. Morejudo, R. Zanón, S. Escolástico, I. Yuste-Tirados, H. Malerød-Fjeld, P. K. Vestre, W. G. Coors, A. Martínez, T. Norby, J. M. Serra, and C. Kjølseth, "Direct conversion of methane to aromatics in a catalytic co-ionic membrane reactor.," *Science*, vol. 353, pp. 563–6, aug 2016.

[22] S. J. Davis, N. S. Lewis, M. Shaner, S. Aggarwal, D. Arent, I. L. Azevedo, S. M. Benson, T. Bradley, J. Brouwer, Y.-M. Chiang, C. T. M. Clack, A. Cohen, S. Doig, J. Edmonds, P. Fennell, C. B. Field, B. Hannegan, B.-M. Hodge, M. I. Hoffert, E. Ingersoll, P. Jaramillo, K. S. Lackner, K. J. Mach, M. Mastrandrea, J. Ogden, F. Peterson, D. L. Sanchez, D. Sperling, J. Stagner, J. E. Trancik, C.-J. Yang, and K. Caldeira, "REVIEW SUMMARY Net-zero emissions energy systems," *Science*, vol. 360, no. 6396, 2018.

[23] S. Dunn, "Hydrogen futures: toward a sustainable energy system," *Int. J. Hydrogen Energy*, vol. 27, pp. 235–264, mar 2002.

[24] N. Mahato, A. Banerjee, A. Gupta, S. Omar, and K. Balani, "Progress in material selection for solid oxide fuel cell technology: A review," *Prog. Mater. Sci.*, vol. 72, pp. 141–337, 2015.

[25] L. Bi and E. Traversa, "Synthesis strategies for improving the performance of doped-$BaZrO_3$ materials in solid oxide fuel cell applications," *J. Mater. Res.*, vol. 29, pp. 1–15, jan 2014.

[26] J. A. Kilner and M. Burriel, "Materials for Intermediate-Temperature Solid-Oxide Fuel Cells," *Annu. Rev. Mater. Res.*, vol. 44, pp. 365–393, jul 2014.

[27] E. Fabbri, L. Bi, D. Pergolesi, and E. Traversa, "Towards the Next Generation of Solid Oxide Fuel Cells Operating Below 600 °C with Chemically Stable Proton-Conducting Electrolytes," *Adv. Mater.*, vol. 24, pp. 195–208, jan 2012.

[28] E. D. Wachsman and K. T. Lee, "Lowering the temperature of solid oxide fuel cells.," *Science*, vol. 334, pp. 935–9, nov 2011.

[29] E. Fabbri, D. Pergolesi, and E. Traversa, "Materials challenges toward proton-conducting oxide fuel cells: a critical review.," *Chem. Soc. Rev.*, vol. 39, pp. 4355–69, nov 2010.

[30] H. Iwahara, T. Yajima, T. Hibino, K. Ozaki, and H. Suzuki, "Protonic conduction in calcium, strontium and barium zirconates," *Solid State Ionics*, vol. 61, pp. 65–69, may 1993.

[31] K. Kreuer, S. Adams, W. Münch, A. Fuchs, U. Klock, and J. Maier, "Proton conducting alkaline earth zirconates and titanates for high drain electrochemical applications," *Solid State Ionics*, vol. 145, pp. 295–306, dec 2001.

[32] R. Hempelmann, "Quasielastic neutron scattering study of proton diffusion in $SrCe_{0.95}Yb_{0.05}H_{0.02}O_{2.985}$," *Solid State Ionics*, vol. 77, pp. 152–156, apr 1995.

[33] T. Matzke, U. Stimming, C. Karmonik, M. Soetratmo, R. Hempelmann, and F. Güthoff, "Quasielastic thermal neutron scattering experiment on the proton conductor $SrCe_{0.95}Yb_{0.05}H_{0.02}O_{2.985}$," *Solid State Ionics*, vol. 86-88, pp. 621–628, jul 1996.

[34] R. Hempelmann, M. Soetratmo, O. Hartmann, and R. Wäppling, "Muon diffusion and trapping in proton conducting oxides," *Solid State Ionics*, vol. 107, pp. 269–280, apr 1998.

[35] Y. Yamazaki, F. Blanc, Y. Okuyama, L. Buannic, J. C. Lucio-Vega, C. P. Grey, and S. M. Haile, "Proton trapping in yttrium-doped barium zirconate.," *Nat. Mater.*, vol. 12, pp. 647–51, jul 2013.

[36] L. Buannic, F. Blanc, I. Hung, Z. Gan, and C. P. Grey, "Probing the local structures and protonic conduction pathways in scandium substituted $BaZrO_3$ by multinuclear solid-state NMR spectroscopy," *J. Mater. Chem.*, vol. 20, no. 30, p. 6322, 2010.

[37] M. E. Björketun, P. G. Sundell, and G. Wahnström, "Effect of acceptor dopants on the proton mobility in $BaZrO_3$: A density functional investigation," *Phys. Rev. B*, vol. 76, p. 054307, aug 2007.

[38] M. E. Björketun, P. G. Sundell, and G. Wahnström, "Effect of acceptor dopants on the proton mobility in $BaZrO_3$: A density functional investigation," *Phys. Rev. B*, vol. 76, p. 054307, aug 2007.

[39] Q. Zhang, G. Wahnström, M. E. Björketun, S. Gao, and E. Wang, "Path integral treatment of proton transport processes in $BaZrO_3$.," *Phys. Rev. Lett.*, vol. 101, p. 215902, nov 2008.

[40] A. Braun and Q. Chen, "Experimental neutron scattering evidence for proton polaron in hydrated metal oxide proton conductors," *Nat. Commun.*, 2017.

[41] M. A. Gomez, M. Chunduru, L. Chigweshe, L. Foster, S. J. Fensin, K. M. Fletcher, and L. E. Fernandez, "The effect of yttrium dopant on the proton conduction pathways of $BaZrO_3$, a cubic perovskite," *J. Chem. Phys.*, vol. 132, p. 214709, jun 2010.

[42] A. Sakurai, K. Ando, and S. Ashihara, "Ultrafast proton/deuteron dynamics in $KTaO_3$ observed with infrared pump-probe spectroscopy: Toward understanding of proton conduction mechanism in solid oxides," *J. Chem. Phys.*, vol. 149, p. 104502, sep 2018.

[43] D. Beckel, A. Bieberle-Hütter, A. Harvey, A. Infortuna, U. Muecke, M. Prestat, J. L. M. Rupp, and L. Gauckler, "Thin films for micro solid oxide fuel cells," *J. Power Sources*, vol. 173, pp. 325–345, nov 2007.

[44] E. Traversa, "Toward the miniaturization of solid oxide fuel cells," *Electrochem. Soc. Interface*, vol. 18, no. 3, p. 49, 2009.

[45] K. Bae, D. Y. Jang, H. J. Choi, D. Kim, J. Hong, B.-K. Kim, J.-H. Lee, J.-W. Son, and J. H. Shim, "Demonstrating the potential of yttrium-doped barium zirconate electrolyte for high-performance fuel cells," *Nat. Commun.*, vol. 8, p. 14553, feb 2017.

[46] D. Pergolesi, E. Fabbri, A. D'Epifanio, E. Di Bartolomeo, A. Tebano, S. Sanna, S. Licoccia, G. Balestrino, and E. Traversa, "High proton conduction in grain-boundary-free yttrium-doped barium zirconate films grown by pulsed laser deposition.," *Nat. Mater.*, vol. 9, pp. 846–52, oct 2010.

[47] Y. B. Kim, T. M. Gür, H.-J. Jung, S. Kang, R. Sinclair, and F. B. Prinz, "Effect of crystallinity on proton conductivity in yttrium-doped barium zirconate thin films," *Solid State Ionics*, vol. 198, pp. 39–46, sep 2011.

[48] J. H. Shim, T. M. Gür, and F. B. Prinz, "Proton conduction in thin film yttrium-doped barium zirconate," *Appl. Phys. Lett.*, vol. 92, p. 253115, jun 2008.

[49] T. Higuchi, T. Owaku, Y. Iida, E. Sakai, M. Kobayashi, and H. Kumigashira, "Proton conduction of $BaCe_{0.90}Y_{0.10}O_{3-\delta}$ thin film with lattice distortion," *Solid State Ionics*, vol. 270, pp. 1–5, feb 2015.

[50] A. Fluri, A. Marcolongo, V. Roddatis, A. Wokaun, D. Pergolesi, N. Marzari, and T. Lippert, "Enhanced Proton Conductivity in Y-Doped $BaZrO_3$ via Strain Engineering," *Adv. Sci.*, vol. 4, p. 1700467, dec 2017.

[51] Y. Kobayashi, O. J. Hernandez, T. Sakaguchi, T. Yajima, T. Roisnel, Y. Tsujimoto, M. Morita, Y. Noda, Y. Mogami, A. Kitada, M. Ohkura, S. Hosokawa, Z. Li, K. Hayashi, Y. Kusano, J. eun Kim, N. Tsuji, A. Fujiwara, Y. Matsushita, K. Yoshimura, K. Takegoshi, M. Inoue, M. Takano, and H. Kageyama, "An oxyhydride of $BaTiO_3$ exhibiting hydride exchange and electronic conductivity," *Nat. Mater.*, vol. 11, pp. 507–511, jun 2012.

[52] T. Sakaguchi, Y. Kobayashi, T. Yajima, M. Ohkura, C. Tassel, F. Takeiri, S. Mitsuoka, H. Ohkubo, T. Yamamoto, J. eun Kim, N. Tsuji, A. Fujihara, Y. Matsushita, J. Hester, M. Avdeev, K. Ohoyama, and H. Kageyama, "Oxyhydrides of (Ca,Sr,Ba)TiO_3 Perovskite Solid Solutions," *Inorg. Chem.*, vol. 51, pp. 11371–11376, nov 2012.

[53] H. Kageyama, K. Hayashi, K. Maeda, J. P. Attfield, Z. Hiroi, J. M. Rondinelli, and K. R. Poeppelmeier, "Expanding frontiers in materials chemistry and physics with multiple anions," *Nat. Commun.*, vol. 9, p. 772, dec 2018.

[54] R. J. D. Tilley, *Perovskites : Structure-Property Relationships*. John Wiley & Sons, Incorporated, 1 ed., 2016.

[55] C. Moure and O. Peña, "Recent advances in perovskites: Processing and properties," *Prog. Solid State Chem.*, vol. 43, no. 4, pp. 123–148, 2015.

[56] E. Kendrick and P. R. Slater, "Battery and solid oxide fuel cell materials," *Annu. Reports Sect. "A" (Inorganic Chem.*, vol. 109, no. 0, p. 396, 2013.

[57] Y. Iwazaki, T. Suzuki, Y. Mizuno, and S. Tsuneyuki, "Doping-induced phase transitions in ferroelectric $BaTiO_3$ from first-principles calculations," *Phys. Rev. B*, vol. 86, p. 214103, dec 2012.

[58] D. G. Thomas and J. J. Lander, "Hydrogen as a Donor in Zinc Oxide," *J. Chem. Phys.*, vol. 25, pp. 1136–1142, dec 1956.

[59] H. Iwahara, T. Esaka, H. Uchida, and N. Maeda, "Proton conduction in sintered oxides and its application to steam electrolysis for hydrogen production," *Solid State Ionics*, vol. 3-4, pp. 359–363, aug 1981.

[60] H. Iwahara, H. Uchida, and S. Tanaka, "High temperature type proton conductor based on $SrCeO_3$ and its application to solid electrolyte fuel cells," *Solid State Ionics*, vol. 9-10, pp. 1021–1025, dec 1983.

[61] H. Iwahara, T. Esaka, H. Uchida, T. Yamauchi, and K. Ogaki, "High temperature type protonic conductor based on $SrCeO_3$ and its application to the extraction of hydrogen gas," *Solid State Ionics*, vol. 18-19, pp. 1003–1007, jan 1986.

[62] H. Iwahara, "Proton Conduction in Sintered Oxides Based on $BaCeO_3$," *J. Electrochem. Soc.*, vol. 135, p. 529, feb 1988.

[63] K. Kreuer, "PROTON-CONDUCTING OXIDES," *Annu. Rev. Mater. Res.*, vol. 33, pp. 333–359, aug 2003.

[64] K. Kreuer, "Aspects of the formation and mobility of protonic charge carriers and the stability of perovskite-type oxides," *Solid State Ionics*, vol. 125, pp. 285–302, oct 1999.

[65] D. Han, Y. Nose, K. Shinoda, and T. Uda, "Site selectivity of dopants in $BaZr_{1-y}M_yO_{3-\delta}$ (M = Sc, Y, Sm, Eu, Dy) and measurement of their water contents and conductivities," *Solid State Ionics*, vol. 213, pp. 2–7, apr 2012.

[66] D. Han, K. Shinoda, S. Sato, M. Majima, and T. Uda, "Correlation between electroconductive and structural properties of proton conductive acceptor-doped barium zirconate," *J. Mater. Chem. A*, vol. 3, pp. 1243–1250, dec 2015.

[67] M. Karlsson, P. Fouquet, I. Ahmed, and M. Maccarini, "Dopant Concentration and Short-Range Structure Dependence of Diffusional Proton

Dynamics in Hydrated $BaIn_xZr_{1-x}O_{3-x/2}$ ($x = 0.10$ and 0.50)," *J. Phys. Chem. C*, vol. 114, pp. 3292–3296, feb 2010.

[68] M. Karlsson, D. Engberg, M. E. Björketun, A. Matic, G. Wahnström, P. G. Sundell, P. Berastegui, I. Ahmed, P. Falus, B. Farago, L. Börjesson, and S.-G. Eriksson, "Using Neutron SpinEcho To Investigate Proton Dynamics in Proton-Conducting Perovskites ," *Chem. Mater.*, vol. 22, pp. 740–742, feb 2010.

[69] M. Karlsson, "Proton dynamics in oxides: insight into the mechanics of proton conduction from quasielastic neutron scattering.," *Phys. Chem. Chem. Phys.*, vol. 17, pp. 26–38, jan 2015.

[70] D. Noferini, M. M. Koza, P. Fouquet, G. J. Nilsen, M. C. Kemei, S. M. H. Rahman, M. Maccarini, S. Eriksson, and M. Karlsson, "Proton Dynamics in Hydrated $BaZr_{0.9}M_{0.1}O_{2.95}$ (M = Y and Sc) Investigated with Neutron Spin-Echo," *J. Phys. Chem. C*, vol. 120, pp. 13963–13969, jul 2016.

[71] L. Buannic, L. Sperrin, R. Dervişoğlu, F. Blanc, and C. P. Grey, "Proton distribution in Sc-doped $BaZrO_3$: a solid state NMR and first principle calculations analysis," *Phys. Chem. Chem. Phys.*, vol. 20, pp. 4317–4328, feb 2018.

[72] I. Oikawa and H. Takamura, "Correlation among Oxygen Vacancies, Protonic Defects, and the Acceptor Dopant in Sc-Doped $BaZrO_3$ Studied by ^{45}Sc Nuclear Magnetic Resonance," *Chem. Mater.*, vol. 27, pp. 6660–6667, oct 2015.

[73] M. Karlsson, M. E. Björketun, P. G. Sundell, A. Matic, G. Wahnström, D. Engberg, L. Börjesson, I. Ahmed, S. Eriksson, and P. Berastegui, "Vibrational properties of protons in hydrated $BaIn_xZr_{1-x}O_{3-x/2}$," *Phys. Rev. B*, vol. 72, p. 094303, sep 2005.

[74] M. Karlsson, A. Matic, S. F. Parker, I. Ahmed, L. Börjesson, and S. Eriksson, "O-H wag vibrations in hydrated $BaIn_xZr_{1-x}O_{3-x/2}$ investigated with inelastic neutron scattering," *Phys. Rev. B*, vol. 77, p. 104302, mar 2008.

[75] M. Karlsson, A. Matic, C. Knee, I. Ahmed, S. Eriksson, and L. Börjesson, "Short-Range Structure of Proton-Conducting Perovskite $BaIn_xZr_{1-x}O_{3-x/2}$ ($x = 0$–0.75)," *Chem. Mater.*, vol. 20, pp. 3480–3486, may 2008.

[76] M. Karlsson, I. Ahmed, A. Matic, and S.-G. Eriksson, "Short-range structure of proton-conducting $BaM_{0.10}Zr_{0.90}O_{2.95}$ (M=Y, In, Sc and Ga) investigated with vibrational spectroscopy," *Solid State Ionics*, vol. 181, pp. 126–129, feb 2010.

[77] J. Bielecki, S. F. Parker, L. Mazzei, L. Börjesson, and M. Karlsson, "Structure and dehydration mechanism of the proton conducting oxide $Ba_2In_2O_5(H_2O)_x$," *J. Mater. Chem. A*, vol. 4, pp. 1224–1232, 2016.

[78] C. W. Mburu, S. M. Gaita, C. S. Knee, M. J. Gatari, and M. Karlsson, "Influence of Yttrium Concentration on Local Structure in $BaZr_{1-x}Y_xO_{3-\delta}$ Based Proton Conductors," *J. Phys. Chem. C*, p. acs.jpcc.7b05023, jul 2017.

[79] P. Haro-González, M. Karlsson, S. Gaita, C. Knee, and M. Bettinelli, "Eu^{3+} as a luminescent probe for the local structure of trivalent dopant ions in barium zirconate-based proton conductors," *Solid State Ionics*, vol. 247-248, pp. 94–97, oct 2013.

[80] W. Münch, G. Seifert, K. Kreuer, and J. Maier, "A quantum molecular dynamics study of proton conduction phenomena in $BaCeO_3$," *Solid State Ionics*, vol. 86-88, pp. 647–652, jul 1996.

[81] W. Münch, G. Seifert, K. Kreuer, and J. Maier, "A quantum molecular dynamics study of the cubic phase of $BaTiO_3$ and $BaZrO_3$," *Solid State Ionics*, vol. 97, pp. 39–44, may 1997.

[82] M. A. Gomez, M. A. Griffin, S. Jindal, K. D. Rule, and V. R. Cooper, "The effect of octahedral tilting on proton binding sites and transition states in pseudo-cubic perovskite oxides," *J. Chem. Phys.*, vol. 123, p. 094703, sep 2005.

[83] M. E. Björketun, P. G. Sundell, and G. Wahnström, "Structure and thermodynamic stability of hydrogen interstitials in $BaZrO_3$ perovskite oxide from density functional calculations," *Faraday Discuss.*, vol. 134, pp. 247–265, dec 2007.

[84] P. G. Sundell, M. E. Björketun, and G. Wahnström, "Density-functional calculations of prefactors and activation energies for H diffusion in $BaZrO_3$," *Phys. Rev. B*, vol. 76, p. 094301, sep 2007.

[85] S. J. Stokes and M. S. Islam, "Defect chemistry and proton-dopant association in $BaZrO_3$ and $BaPrO_3$," *J. Mater. Chem.*, vol. 20, p. 6258, jul 2010.

[86] P. Raiteri, J. D. Gale, and G. Bussi, "Reactive force field simulation of proton diffusion in $BaZrO_3$ using an empirical valence bond approach," *J. Phys. Condens. Matter*, vol. 23, p. 334213, aug 2011.

[87] N. Kitamura, J. Akola, S. Kohara, K. Fujimoto, and Y. Idemoto, "Proton Distribution and Dynamics in Y- and Zn-Doped $BaZrO_3$," *J. Phys. Chem. C*, vol. 118, pp. 18846–18852, aug 2014.

[88] D. Zeudmi Sahraoui and T. Mineva, "Effect of dopant nature on structures and lattice dynamics of proton-conducting $BaZrO_3$," *Solid State Ionics*, vol. 253, pp. 195–200, dec 2013.

[89] M. A. Gomez, G. Kwan, W. Zhu, M. Chelliah, X. Zuo, A. Eshun, V. Blackmer, T. Huynh, and M. Huynh, "Ordered yttrium concentration effects on barium zirconate structure, proton binding sites and transition states," *Solid State Ionics*, vol. 304, pp. 126–134, 2017.

[90] M. A. Gomez, D. L. Fry, and M. E. Sweet, "Effects on the Proton Conduction Limiting Barriers and Trajectories in $BaZr_{0.875}Y_{0.125}O_3$ Due to the Presence of Other Protons," *J. Korean Ceram. Soc.*, vol. 53, pp. 521–528, sep 2016.

[91] K. Toyoura, W. Meng, D. Han, and T. Uda, "Preferential proton conduction along a three-dimensional dopant network in yttrium-doped barium zirconate: a first-principles study," *J. Mater. Chem. A*, vol. 6, pp. 22721–22730, nov 2018.

[92] K. Kreuer, "On the development of proton conducting materials for technological applications," *Solid State Ionics*, vol. 97, pp. 1–15, may 1997.

[93] I. Ahmed, S. Eriksson, E. Ahlberg, C. Knee, P. Berastegui, L. Johansson, H. Rundlöf, M. Karlsson, A. Matic, and L. Börjesson, "Synthesis and structural characterization of perovskite type proton conducting $BaZr_{1-x}In_xO_{3-\delta}$ $(0.0 \leq x \leq 0.75)$," *Solid State Ionics*, vol. 177, pp. 1395–1403, jul 2006.

[94] I. Ahmed, S. Eriksson, E. Ahlberg, C. Knee, L. Johansson, M. Karlsson, A. Matic, L. Börjesson, and H. Götlind, "Structural study and proton

conductivity in Yb-doped $BaZrO_3$," *Solid State Ionics*, vol. 178, pp. 515–520, apr 2007.

[95] I. Ahmed, M. Karlsson, S. Eriksson, E. Ahlberg, C. Knee, K. Larsson, A. K. Azad, A. Matic, and L. Börjesson, "Crystal Structure and Proton Conductivity of $BaZr_{0.9}Sc_{0.1}O_{3-\delta}$," *J. Am. Ceram. Soc.*, vol. 91, pp. 3039–3044, sep 2008.

[96] F. Giannici, A. Longo, A. Balerna, K. Kreuer, and A. Martorana, "Proton Dynamics in In:$BaZrO_3$: Insights on the Atomic and Electronic Structure from X-ray Absorption Spectroscopy," *Chem. Mater.*, vol. 21, pp. 2641–2649, jul 2009.

[97] E. Fabbri, D. Pergolesi, S. Licoccia, and E. Traversa, "Does the increase in Y-dopant concentration improve the proton conductivity of $BaZr_{1-x}Y_xO_{3-\delta}$ fuel cell electrolytes?," *Solid State Ionics*, vol. 181, pp. 1043–1051, jul 2010.

[98] C. J. T. de Grotthuss, "Mémoire sur la décomposition de l'eau et des corps qu'elle tient en dissolution à l'aide de l'électricité galvanique," *Ann. Chim.*, no. LVIII, p. 54, 1806.

[99] D.-H. Kim, B.-K. Kim, and Y.-C. Kim, "Energy barriers for proton migration in yttrium-doped barium zirconate super cell with $\Sigma 5$ (310)/[001] tilt grain boundary," *Solid State Ionics*, vol. 213, pp. 18–21, apr 2012.

[100] I. Ahmed, C. Knee, M. Karlsson, S. Eriksson, P. F. Henry, A. Matic, D. Engberg, and L. Börjesson, "Location of deuteron sites in the proton conducting perovskite $BaZr_{0.50}In_{0.50}O_{3-\delta}$," *J. Alloys Compd.*, vol. 450, pp. 103–110, feb 2008.

[101] D. Noferini, M. M. Koza, and M. Karlsson, "Localized Proton Motions in Acceptor-Doped Barium Zirconates," *J. Phys. Chem. C*, vol. 121, pp. 7088–7093, apr 2017.

[102] D. Noferini, M. M. Koza, S. M. H. Rahman, Z. Evenson, G. J. Nilsen, S. Eriksson, A. R. Wildes, and M. Karlsson, "Role of the doping level in localized proton motions in acceptor-doped barium zirconate proton conductors," *Phys. Chem. Chem. Phys.*, vol. 20, pp. 13697–13704, may 2018.

[103] M. Glerup, "Vibrational spectroscopy on protons and deuterons in proton conducting perovskites," *Solid State Ionics*, vol. 148, pp. 83–92, may 2002.

[104] M. Karlsson, A. Matic, E. Zanghellini, and I. Ahmed, "Temperature-Dependent Infrared Spectroscopy of Proton-Conducting Hydrated Perovskite $BaIn_xZr_{1-x}O_{1-x/2}$ ($x = 0.10$–0.75)," *J. Phys. Chem. C*, vol. 114, pp. 6177–6181, apr 2010.

[105] J.-R. Martinez, C. E. Mohn, S. Stølen, and N. L. Allan, "$Ba_2In_2O_4(OH)_2$: Proton sites, disorder and vibrational properties," *J. Solid State Chem.*, vol. 180, no. 12, pp. 3388–3392, 2007.

[106] E. Libowitzky, "Correlation of O-H stretching frequencies and O-H...O hydrogen bond lengths in minerals," *Monatshefte für Chemie / Chem. Mon.*, vol. 130, pp. 1047–1059, may 2015.

[107] J. T. Last, "Infrared-Absorption Studies on Barium Titanate and Related Materials," *Phys. Rev.*, vol. 105, pp. 1740–1750, mar 1957.

[108] I. Ahmed, S. Eriksson, E. Ahlberg, C. Knee, M. Karlsson, A. Matic, L. Börjesson, and D. Engberg, "Proton conductivity and low temperature structure of In-doped $BaZrO_3$," *Solid State Ionics*, vol. 177, pp. 2357–2362, oct 2006.

[109] I. Ahmed, S.-G. Eriksson, E. Ahlberg, and C. S. Knee, "Influence of microstructure on electrical properties in $BaZr_{0.5}In_{0.5}O_{3-\delta}$ proton conductor," *Solid State Ionics*, vol. 179, no. 21, pp. 1155–1160, 2008.

[110] E. Gilardi, E. Fabbri, L. Bi, J. L. M. Rupp, T. Lippert, D. Pergolesi, and E. Traversa, "Effect of Dopant Host Ionic Radii Mismatch on Acceptor-Doped Barium Zirconate Microstructure and Proton Conductivity," *J. Phys. Chem. C*, vol. 121, pp. 9739–9747, may 2017.

[111] F. Giannici, A. Longo, K. Kreuer, A. Balerna, and A. Martorana, "Dopants and defects: Local structure and dynamics in barium cerates and zirconates," *Solid State Ionics*, vol. 181, pp. 122–125, feb 2010.

[112] F. Giannici, M. Shirpour, A. Longo, A. Martorana, R. Merkle, and J. Maier, "Long-Range and Short-Range Structure of Proton-Conducting Y:$BaZrO_3$," *Chem. Mater.*, vol. 23, pp. 2994–3002, jun 2011.

[113] D. Noferini, B. Frick, M. M. Koza, and M. Karlsson, "Proton jump diffusion dynamics in hydrated barium zirconates studied by high-resolution neutron backscattering spectroscopy," *J. Mater. Chem. A*, vol. 6, pp. 7538–7546, may 2018.

[114] M. E. Björketun, P. G. Sundell, G. Wahnström, and D. Engberg, "A kinetic Monte Carlo study of proton diffusion in disordered perovskite structured lattices based on first-principles calculations," *Solid State Ionics*, vol. 176, pp. 3035–3040, dec 2005.

[115] E. Jedvik, A. Lindman, M. . Benediktsson, and G. Wahnström, "Size and shape of oxygen vacancies and protons in acceptor-doped barium zirconate," *Solid State Ionics*, vol. 275, pp. 2–8, 2015.

[116] N. Bork, N. Bonanos, J. Rossmeisl, and T. Vegge, "Ab initio charge analysis of pure and hydrogenated perovskites," *J. Appl. Phys.*, vol. 109, p. 033702, feb 2011.

[117] T. S. Bjørheim, M. Arrigoni, D. Gryaznov, E. Kotomin, and J. Maier, "Thermodynamic properties of neutral and charged oxygen vacancies in $BaZrO_3$ based on first principles phonon calculations," *Phys. Chem. Chem. Phys.*, vol. 17, pp. 20765–20774, aug 2015.

[118] T. S. Bjørheim, A. Løken, and R. Haugsrud, "On the relationship between chemical expansion and hydration thermodynamics of proton conducting perovskites," *J. Mater. Chem. A*, vol. 4, no. 16, pp. 5917–5924, 2016.

[119] H.-S. Kim, A. Jang, S.-Y. Choi, W. Jung, and S.-Y. Chung, "Vacancy-Induced Electronic Structure Variation of Acceptors and Correlation with Proton Conduction in Perovskite Oxides," *Angew. Chemie*, aug 2016.

[120] C. Kjølseth, H. Fjeld, Ø. Prytz, P. Dahl, C. Estournès, R. Haugsrud, and T. Norby, "Spacecharge theory applied to the grain boundary impedance of proton conducting $BaZr_{0.9}Y_{0.1}O_{3-\delta}$," *Solid State Ionics*, vol. 181, pp. 268–275, mar 2010.

[121] M. Shirpour, B. Rahmati, W. Sigle, P. A. van Aken, R. Merkle, and J. Maier, "Dopant Segregation and Space Charge Effects in Proton-Conducting $BaZrO_3$ Perovskites," *J. Phys. Chem. C*, vol. 116, pp. 2453–2461, jan 2012.

[122] M. Shirpour, R. Merkle, C. T. Lin, and J. Maier, "Nonlinear electrical grain boundary properties in proton conducting Y-$BaZrO_3$ supporting the space charge depletion model," *Phys. Chem. Chem. Phys.*, vol. 14, no. 2, pp. 730–740, 2012.

[123] C.-T. Chen, C. E. Danel, and S. Kim, "On the origin of the blocking effect of grain-boundaries on proton transport in yttrium-doped barium zirconates," *J. Mater. Chem.*, vol. 21, no. 14, p. 5435, 2011.

[124] Y. Yamazaki, R. Hernandez-Sanchez, and S. M. Haile, "Cation non-stoichiometry in yttrium-doped barium zirconate: phase behavior, microstructure, and proton conductivity," *J. Mater. Chem.*, vol. 20, p. 8158, sep 2010.

[125] D. Han, K. Kishida, H. Inui, and T. Uda, "Substantial appearance of origin of conductivity decrease in Y-doped $BaZrO_3$ due to Ba-deficiency," *RSC Adv.*, vol. 4, p. 31589, jul 2014.

[126] A. Lindman, T. S. Bjørheim, G. Wahnström, J. Maier, B. P. Gorman, R. P. O'Hayre, T. Norby, J. M. Serra, and C. Kjølseth, "Defect segregation to grain boundaries in $BaZrO_3$ from first-principles free energy calculations," *J. Mater. Chem. A*, vol. 5, pp. 13421–13429, jul 2017.

[127] B. Groß, C. Beck, F. Meyer, T. Krajewski, R. Hempelmann, and H. Altgeld, "$BaZr_{0.85}Me_{0.15}O_{2.925}$ (Me=Y, In and Ga): crystal growth, high-resolution transmission electron microscopy, high-temperature X-ray diffraction and neutron scattering experiments," *Solid State Ionics*, vol. 145, no. 1, pp. 325–331, 2001.

[128] B. Malaman and J. Brice, "Etude structurale de l'hydruro-oxyde LaHO par diffraction des rayons X et par diffraction des neutrons," *J. Solid State Chem.*, vol. 53, pp. 44–54, jun 1984.

[129] V. N. Fokin, E. E. Fokina, I. I. Korobov, and B. P. Tarasov, "Hydrogenation of Zr_3Al_2 in hydrogen and ammonia," *Inorg. Mater.*, vol. 49, pp. 145–148, feb 2013.

[130] B. Huang and J. D. Corbett, "$Ba_{21}Ge_2O_5H_{24}$ and Related Phases. A Corrected Structure Type and Composition for a Zintl Phase Stabilized by Hydrogen," *Inorg. Chem.*, vol. 37, no. 8, pp. 1892–1899, 1998.

[131] B. Huang and J. D. Corbett, "Ba_3AlO_4H: Synthesis and Structure of a New Hydrogen-Stabilized Phase," *J. Solid State Chem.*, vol. 141, pp. 570–575, dec 1998.

[132] R. M. Helps, N. H. Rees, and M. A. Hayward, "$Sr_3Co_2O_{4.33}H_{0.84}$: An Extended Transition Metal Oxide-Hydride," *Inorg. Chem.*, vol. 49, pp. 11062–11068, dec 2010.

[133] K. Hayashi, S. Matsuishi, T. Kamiya, M. Hirano, and H. Hosono, "Light-induced conversion of an insulating refractory oxide into a persistent electronic conductor," *Nature*, vol. 419, pp. 462–465, oct 2002.

[134] M. A. Hayward, E. J. Cussen, J. B. Claridge, M. Bieringer, M. J. Rosseinsky, C. J. Kiely, S. J. Blundell, I. M. Marshall, and F. L. Pratt, "The Hydride Anion in an Extended Transition Metal Oxide Array: $LaSrCoO_3H_{0.7}$," *Science (80-.).*, vol. 295, pp. 1882–1884, mar 2002.

[135] Y. Kobayashi, Y. Tsujimoto, and H. Kageyama, "Property Engineering in Perovskites via Modification of Anion Chemistry," *Annu. Rev. Mater. Res.*, vol. 48, pp. 303–326, jul 2018.

[136] R. Nedumkandathil, A. Jaworski, J. Grins, D. Bernin, M. Karlsson, C. Eklöf-Österberg, A. Neagu, C.-W. Tai, A. J. Pell, and U. Häussermann, "Hydride Reduction of $BaTiO_3$ - Oxyhydride Versus O Vacancy Formation," *ACS Omega*, vol. 3, pp. 11426–11438, sep 2018.

[137] Y. Iwazaki, T. Suzuki, and S. Tsuneyuki, "Negatively charged hydrogen at oxygen-vacancy sites in $BaTiO_3$: Density-functional calculation," *J. Appl. Phys.*, vol. 108, p. 083705, oct 2010.

[138] X. Liu, T. S. Bjørheim, and R. Haugsrud, "Formation and migration of hydride ions in $BaTiO_{3-x}H_x$ oxyhydride," *J. Mater. Chem. A*, vol. 5, pp. 1050–1056, jan 2017.

[139] J. Zhang, G. Gou, and B. Pan, "Study of Phase Stability and Hydride Diffusion Mechanism of $BaTiO_3$ Oxyhydride from First-Principles," *J. Phys. Chem. C*, vol. 118, pp. 17254–17259, aug 2014.

[140] M. Schrader, D. Mienert, T.-S. Oh, H.-I. Yoo, and K. D. Becker, "An optical, EPR and electrical conductivity study of blue barium titanate, $BaTiO_{3-\delta}$," *Solid State Sci.*, vol. 10, pp. 768–775, jun 2008.

[141] G. Kobayashi, Y. Hinuma, S. Matsuoka, A. Watanabe, M. Iqbal, M. Hirayama, M. Yonemura, T. Kamiyama, I. Tanaka, and R. Kanno, "Pure H^- conduction in oxyhydrides.," *Science*, vol. 351, pp. 1314–7, mar 2016.

[142] F. Takeiri, K. Aidzu, T. Yajima, T. Matsui, T. Yamamoto, Y. Kobayashi, J. Hester, and H. Kageyama, "Promoted Hydride/Oxide Exchange in $SrTiO_3$ by Introduction of Anion Vacancy via Aliovalent Cation Substitution," *Inorg. Chem.*, vol. 56, pp. 13035–13040, nov 2017.

[143] R. Mikita, T. Aharen, T. Yamamoto, F. Takeiri, T. Ya, W. Yoshimune, K. Fujita, S. Yoshida, K. Tanaka, D. Batuk, A. M. Abakumov, C. M. Brown, Y. Kobayashi, and H. Kageyama, "Topochemical Nitridation with Anion Vacancy-Assisted N^{3-}/O^{2-} Exchange," *J. Am. Chem. Soc.*, vol. 138, pp. 3211–3217, mar 2016.

[144] Y. Tang, Y. Kobayashi, K. Shitara, A. Konishi, A. Kuwabara, T. Nakashima, C. Tassel, T. Yamamoto, and H. Kageyama, "On Hydride Diffusion in Transition Metal Perovskite Oxyhydrides Investigated via Deuterium Exchange," *Chem. Mater.*, vol. 29, pp. 8187–8194, oct 2017.

[145] C. Eklöf-Österberg, R. Nedumkandathil, U. Häussermann, A. Jaworski, A. J. Pell, M. Tyagi, N. H. Jalarvo, B. Frick, A. Faraone, and M. Karlsson, "Dynamics of Hydride Ions in Metal Hydride-Reduced $BaTiO_3$ Samples Investigated with Quasielastic Neutron Scattering," *J. Phys. Chem. C*, vol. 123, pp. 2019–2030, jan 2019.

[146] T. U. Ito, A. Koda, K. Shimomura, W. Higemoto, T. Matsuzaki, Y. Kobayashi, and H. Kageyama, "Excited configurations of hydrogen in the $BaTiO_{3-x}H_x$ perovskite lattice associated with hydrogen exchange and transport," *Phys. Rev. B*, vol. 95, p. 020301, jan 2017.

[147] S. Lovesey, *Theory of neutron scattering from condensed matter*. 1984.

[148] G. Squires, *Introduction to the Theory of Thermal Neutron Scattering*. Dover Publications, 1978.

[149] P. C. H. Mitchell;, S. F. Parker, A. Ramirez-Cuesta;, and J. Tomkinson, *Vibrational Spectroscopy with Neutrons*. Singapore: Word Scientific, 2005.

[150] V. F. Sears, "Neutron scattering lengths and cross sections," *Neutron News*, vol. 3, pp. 26–37, aug 2006.

[151] J. Tomkinson, M. Warner, and A. Taylor, "Powder averages for neutron spectroscopy of anisotropic molecular oscillators," *Mol. Phys.*, vol. 51, pp. 381–392, aug 2006.

[152] R. Steudel, "Infrared and Raman Spectroscopy. Methods and Applications. Edited by Bernhard Schrader, VCH, Weinheim 1995, XVIII, 787 pp., hardcover, DM 298.00, ISBN 3-527-26446-9," *Adv. Mater.*, vol. 9, pp. 275–276, mar 1997.

[153] N. B. Colthup, L. H. Daly, and S. E. Wiberley, *Introduction to Infrared and Raman Spectroscopy.* Elsevier, 1990.

[154] P. Larkin, *Infrared and Raman Spectroscopy.* Elsevier, 2011.

[155] K. Nakamoto, *Infrared and Raman Spectra of Inorganic and Coordination Compounds: Part A: Theory and Applications in Inorganic Chemistry: Sixth Edition.* 2008.

[156] J. Daillant and A. Gubaud, *X-ray and Neutron Reflectivity*, vol. 770 of *Lecture Notes in Physics.* Berlin, Heidelberg: Springer Berlin Heidelberg, 2009.

[157] M. Björck and G. Andersson, "GenX: an extensible X-ray reflectivity refinement program utilizing differential evolution," *J. Appl. Crystallogr.*, vol. 40, pp. 1174–1178, nov 2007.

[158] L. Parratt, "Surface Studies of Solids by Total Reflection of X-Rays," *Phys. Rev.*, vol. 95, pp. 359–369, jul 1954.

[159] M. Wilde and K. Fukutani, "Hydrogen detection near surfaces and shallow interfaces with resonant nuclear reaction analysis," *Surf. Sci. Rep.*, vol. 69, pp. 196–295, dec 2014.

[160] G. Shirane, S. M. Shapiro, and John M. T., *Neutron Scattering with a Triple-Axis Spectrometer.* Cambridge: Cambridge University Press, 1st ed., 2002.

[161] R. Bewley, R. Eccleston, K. McEwen, S. Hayden, M. Dove, S. M. Bennington, J. Treadgold, and R. Coleman, "MERLIN, a new high count rate spectrometer at ISIS," *Phys. B Condens. Matter*, vol. 385-386, pp. 1029–1031, nov 2006.

[162] S. F. Parker, F. Fernandez-Alonso, A. J. Ramirez-Cuesta, J. Tomkinson, S. Rudic, R. S. Pinna, G. Gorini, and J. Fernández Castañon, "Recent and future developments on TOSCA at ISIS," *J. Phys. Conf. Ser.*, vol. 554, p. 012003, nov 2014.

[163] "VISION, https://neutrons.ornl.gov/vision."

[164] S. F. Parker, A. J. Ramirez-Cuesta, and L. Daemen, "Vibrational spectroscopy with neutrons: Recent developments," *Spectrochim. Acta Part A Mol. Biomol. Spectrosc.*, vol. 190, pp. 518–523, feb 2018.

[165] W. Herres and J. Gronholz, "Understanding FT-IR Data Processing," *J. Comput. Appl. Lab.*, vol. 2, pp. 216–220, 1984.

[166] B. Schulz, J. Bäckström, D. Budelmann, R. Maeser, M. Rübhausen, M. V. Klein, E. Schoeffel, A. Mihill, and S. Yoon, "Fully reflective deep ultraviolet to near infrared spectrometer and entrance optics for resonance Raman spectroscopy," *Rev. Sci. Instrum.*, vol. 76, p. 073107, jul 2005.

[167] "NCNR(NIST): https://www.ncnr.nist.gov/."

[168] J. A. Dura, D. J. Pierce, C. F. Majkrzak, N. C. Maliszewskyj, D. J. McGillivray, M. Lösche, K. V. O'Donovan, M. Mihailescu, U. Perez-Salas, D. L. Worcester, and S. H. White, "AND/R: Advanced neutron diffractometer/reflectometer for investigation of thin films and multilayers for the life sciences.," *Rev. Sci. Instrum.*, vol. 77, pp. 74301–7430111, jul 2006.

[169] "ILL: https://www.ill.eu/."

[170] R. Cubitt and G. Fragneto, "D17: the new reflectometer at the ILL," *Appl. Phys. A Mater. Sci. Process.*, vol. 74, pp. s329–s331, dec 2002.

[171] R. Dervişoğlu, R., D. S. Middlemiss, F. Blanc, Y.-L. Lee, D. Morgan, and C. P. Grey, "Joint Experimental and Computational ^{17}O and 1H Solid State NMR Study of $Ba_2In_2O_4(OH)_2$ Structure and Dynamics," *Chem. Mater.*, vol. 27, pp. 3861–3873, jun 2015.

[172] J. Bielecki, S. F. Parker, D. Ekanayake, S. M. H. Rahman, L. Börjesson, and M. Karlsson, "Short-range structure of the brownmillerite-type oxide $Ba_2In_2O_5$ and its hydrated proton-conducting form $BaInO_3H$," *J. Mater. Chem. A*, vol. 2, pp. 16915–16924, sep 2014.

[173] J. Bielecki, S. F. Parker, L. Mazzei, L. Börjesson, and M. Karlsson, "Structure and dehydration mechanism of the proton conducting oxide $Ba_2In_2O_5(H_2O)x$," *J. Mater. Chem. A*, vol. 4, pp. 1224–1232, 2016.

[174] A. Perrichon, M. Jiménez-Ruiz, L. Mazzei, S. M. H. Rahman, and M. Karlsson, "Proton vibrational dynamics in proton-conducting brownmillerite-based $Ba_2In_2O_5(H_2O)_x$ oxides." Manuscript, 2019.

[175] R. B. Cervera, S. Miyoshi, Y. Oyama, Y. Elammari, T. Yagi, and S. Yamaguchi, "Perovskite-Structured $BaScO_2(OH)$ as a Novel Proton Conductor: Heavily Hydrated Phase Obtained via Low-Temperature Synthesis," *Chem. Mater.*, vol. 25, pp. 1483–1489, may 2013.

[176] C. Beck, S. Janssen, B. Groß, and R. Hempelmann, "Neutron time-of-flight spectrometer FOCUS at SINQ: results from nanocrystalline matter studies," *Scr. Mater.*, vol. 44, no. 8, pp. 2309–2313, 2001.

[177] A. Samgin, "Lattice-assisted proton motion in perovskite oxides," *Solid State Ionics*, vol. 136-137, pp. 291–295, nov 2000.

[178] A. Samgin, "Optically stimulated proton hopping in oxides at low temperatures," *Solid State Commun.*, vol. 152, pp. 585–587, apr 2012.

[179] A. Samgin, "Lattice-assisted proton hopping in oxides at low temperatures," *J. Phys. Chem. Solids*, vol. 74, pp. 1661–1668, dec 2013.

[180] J. Robertson, "Band offsets of wide-band-gap oxides and implications for future electronic devices," *J. Vac. Sci. Technol. B Microelectron. Nanom. Struct. Process. Meas. Phenom.*, vol. 18, p. 1785, jun 2000.

[181] S. Parida, S. K. Rout, L. S. Cavalcante, E. Sinha, M. S. Li, V. Subramanian, N. Gupta, V. R. Gupta, J. A. Varela, and E. Longo, "Structural refinement, optical and microwave dielectric properties of $BaZrO_3$," *Ceram. Int.*, 2012.

[182] R. Borja-Urby, L. A. Diaz-Torres, P. Salas, M. Vega-Gonzalez, and C. Angeles-Chavez, "Blue and red emission in wide band gap $BaZrO_3$:Yb^{3+},Tm^{3+}," *Mater. Sci. Eng. B*, vol. 174, pp. 169–173, oct 2010.

[183] E. C. Aguiar, A. Z. Simões, C. A. Paskocimas, M. Cilense, E. Longo, and J. A. Varela, "Photoluminescence of $BaZrO_3$ explained by a order/disorded transformation," *J. Mater. Sci. Mater. Electron.*, vol. 26, pp. 1993–2001, apr 2015.

[184] L. S. Cavalcante, V. M. Longo, M. Zampieri, J. W. M. Espinosa, P. S. Pizani, J. R. Sambrano, J. A. Varela, E. Longo, M. L. Simões, and C. A. Paskocimas, "Experimental and theoretical correlation of very intense visible green photoluminescence in powders," *J. Appl. Phys*, vol. 103, p. 63527, 2008.